SEARCHING FOR SOLAR AXIONS IN CAST - CERN AXION SOLAR TELESCOPE

by

Özgen Berkol Doğan

B.S. in Physics, Boğaziçi University, 2003

Submitted to the Institute for Graduate Studies in
Science and Engineering in partial fulfillment of
the requirements for the degree of
Master of Science

Graduate Program in Physics

Boğaziçi University

2006

ACKNOWLEDGEMENTS

There have been many people who have supported me and pushed me onwards when I was all ready to turn back, when I was tired and did not trust myself enough. This work is not only mine, but their accomplishment as well. Although I cannot even begin to thank every person that has had a part in my current place, I simply cannot forget some, without whom, I probably would not be a physisict, let alone finish this work.

I wish to thank ...

...Prof Dr. Engin Arık, for making my dream come true,

...Assoc. Prof. Dr. Serkant Çetin, for believing in me when I failed to believe myself,

...Prof. Dr. Metin Arık, for your help in things that seemed to be from another plane of existance,

...My parents, for supporting me in my choices regardless of your own desires,

...Bülay, since you have always been the closest one for me,

...and Hande, for showing me what happiness is...

Of course, I must not forget to mention the wonderful people in the CAST experiment, who have been totally dedicated to their work... Prof. Dr. Konstantin Zioutas, Thomas, Jaime, Nuno, Biljana, and all the others... thank you... For your help, for your patience, for your understanding, for your friendship.

ABSTRACT

SEARCHING FOR SOLAR AXIONS IN CAST - CERN AXION SOLAR TELESCOPE

In this work, a general overview of the CAST experiment is given, and solutions to the specific problems that arose during the preperation time for the Phase II is explained, as well as the steps that were taken to reach the solutions. The analysis procedures of the collected data are also mentioned.

Apart from a theoretical introduction about the axion particle and dark matter, a background on the CERN laboratory is presented as well.

The detectors of CAST are described in detail, with their working principles, geometries, shielding materials, analysis programs and the results obtained from their data collected during the 2003 data taking period.

ÖZET

CERN-CAST DENEYİNDE GÜNEŞTEN GELEN AXION'LARIN ARAŞTIRILMASI

Bu çalışmada CAST deneyinin genel özellikleri verilmiş, deneyin ikinci aşamasına geçme çalışmaları sırasında karşılaşılan problemlerin çözümlerinin yanı sıra bu çözümlere ulaşmak için atılan adımlar açıklanmaya çalışılmıştır. Bunlar dışında detektorlerin analiz programlarina da değinilmiştir.

Axion parçacığı ve karanlik madde üzerine bir girişin yanı sıra CERN laboratuvari hakkinda da bir ön bilgi verilmiştir.

CAST deneyinin detektörleri, çalışma prensipleri, yapıları, kulllanılan zırh malzemeleri, analiz programları ve 2003 veri alma dönemi içinde elde edilen verilerden ulaşılan sonuçlarla, ayrıntılı bir şekilde açıklanmıştır.

TABLE OF CONTENTS

LIST OF FIGURES

LIST OF TABLES

LIST OF SYMBOLS/ABBREVIATIONS

a	Axion
B	Magnetic Field
E	Electric Field
f_{PQ}	Peccei-Quinn Scale
$F^{\alpha\mu\nu}$	Electromagnetic Field Tensor
$g_{a\gamma}$	Axion Photon Coupling Constant
g_s	Strong Coupling Constant
L	Length
$\mathcal{L}$	Lagrangian
m_a	Axion Mass
$\mathcal{M}$	Quark Mass Matrix
p	Proton
$\bar{p}$	Anti-proton
p_a	Axion Momentum
p_γ	Photon Momentum
$P_{a\rightarrow\gamma}$	Axion Photon conversion probability
q	Difference between Axion and Photon momenta
γ	Photon
Γ	Absorbtion Coefficient
ω	Total Energy
ϕ_a	Axion Flux

BEBC	Big European Bubble Chamber
CAST	Cern Axion Solar Telescope
CCD	Charge Coupled Device
CERN	European Organization for Nuclear Research (Conseil Européen pour la Recherche Nucléaire)
COSME	A small, natural abundance, germanium detector
FADC	Flash Analog to Digital Converter

GUI	Graphical User Interface
ISR	Intersecting Storage Rings
LEP	Large Electron-Positron Collider
LHC	Large Hadron Collider
MFB	Magnet Feed Box
MicroMEGAS	Micromesh Gaseous Structure
MRB	Magnet Return Box
NIM	Nuclear Instrumentation Module
PS	Proton Synchrotron
SPS	Super Proton Synchrotron
SOLAX	Solar Axion Experiment
TPC	Time Projection Chamber
VME	Versa Module Eurocard
WIMP	Weakly Interacting Massive Particle
WWW	World Wide Web

1. INTRODUCTION

1.1. CERN

CERN, European Council for Nuclear Research, is stationed in Geneva, on the Swiss/French border. The institution was founded in 1954 by the colloboration of 12 founder states five years after the proposal in 1949 made by Louis de Broglie. Germany, Belgium, Denmark, France, Greece, Italy, Norway, The Netherlands, United Kingdom, Sweden, Switzerland and Yugoslavia were the twelve founding members, however later on, Austria, Bulgaria, Czech and Slovak Republics, Finland, Hungary, Poland, Portugal and Spain joined and Yugoslavia left the organization because of financial reasons later on, making the total number of member states 20[1] as CERN has become one of the world's leading accelarator and particle physics research institute.

The first accelerator of CERN [1], the 600 MeV Synchro-Cyclotron was put into operation in 1957. This was a great success as it enabled the observation of the first pion decay into an electron and a neutrino. 28 GeV Proton Synchrotron (PS) was finished in 1959, which was at that time the most powerful accelerator in the world. In the 60's the first bubble chambers were put into use at CERN and the Intersecting Storage Rings (ISR) construction was approved. Also BEBC (Big European Bubble Chamber) is commissioned. In the 70's ISR produced first of its important discoveries, the wave nature of protons. Also, with the PS and the Gargamelle bubble chamber the "neutral current interaction" was discovered. The Super Proton Synchrotron (SPS) was built and in 1983, W and Z bosons were discovered in $p\bar{p}$ collisions at the SPS. In 1989 Large Electron-Positron collider (LEP) was completed and put into operation until the end of 2000. LEP produced results which indicated that there were only three families of quarks with light neutrinos with the first of these families of quarks and leptons being the building blocks of matter. Lastly, the Large Hadron Collider (LHC) is being built and will start probing the last frontiers of human understanding of matter, in 2007, searching for the source of mass by looking for the Higgs particle

[1]The number of memeber states today

and other new physics like the behavior of matter when the quark/gluon structure is broken.

CERN is also the birth place of the World Wide Web (WWW) which we use as an everyday internet protocol. The WWW was born in order to satisfy the communicational needs of the collaborating scientists, but quickly got popular among the non-scientific community. As of today, another, more powerful network called GRID which will provide computing power and fast data transfer ability for the collaborating scientists to satisfy the large amounts of data transfer needed to study LHC data. This network is already established in some countries but is still tried to be incorporated in others.

1.2. CAST

CAST Experiment [2, 3] is stationed at CERN in LEP point 8, building SR8, and was founded to search for the hypothetical particle known as the axion. While the collaboration was formed in 1999, the actual experiment was approved in 2000, and currently it has got collaborators from Canada, Croatia, France, Germany, Greece, Italy, Russia, Spain, Switzerland, Turkey and the USA.

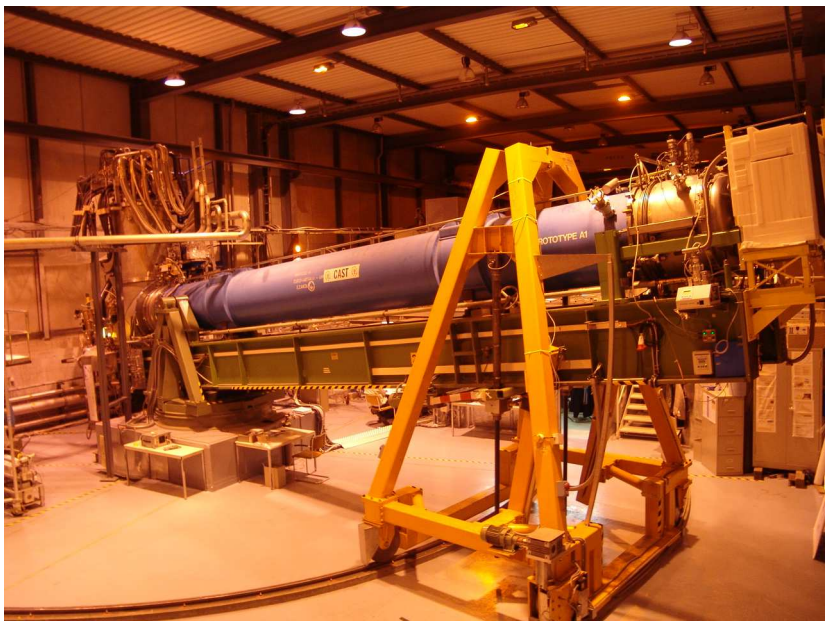

Figure 1.1. The CAST Experiment

The main purpose of the CAST experiment (Figure 1.1) is to detect solar axions by converting them into x-rays within a large magnetic field provided by a decommissioned LHC magnet. The x-ray detection process is conducted by three detectors, MicroMEGAS, CCD and TPC. There are different working groups for each of the detectors and the main components (like cryogenics, pressure, solar tracking) of the magnet.

The experiment uses a 9.3 m, 9.0 Tesla LHC decommissioned prototype magnet for an efficient axion conversion. The magnet tracks the sun during sunrise and sunset, but only up to $\pm 8^o$ from the horizontal[2] . The two sides of the cylindrical magnet there are a total of three detectors, CCD, Micromegas and TPC. Sunrise axions are to be observed by the CCD and the MicroMEGAS, while sunset axions are to be observed by the TPC. The two bores within the magnet are along the magnet length. While TPC covers both of the bores, CCD and MicroMEGAS cover only one bore each (Figure 1.2).

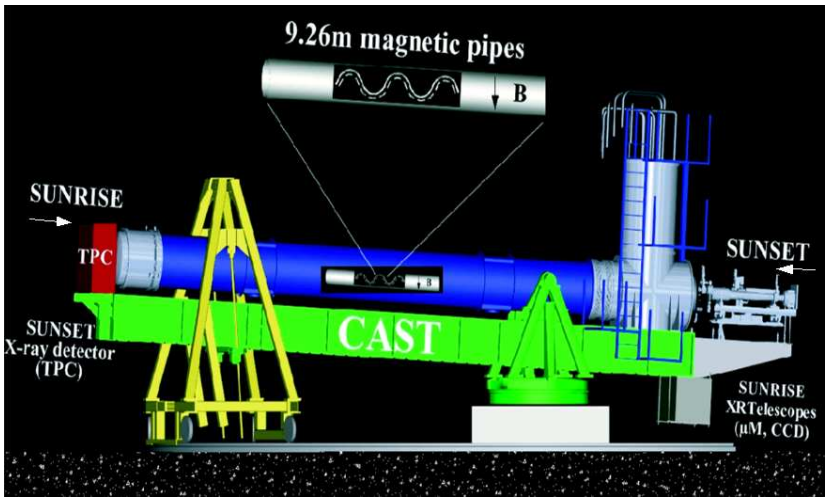

Figure 1.2. A schematic of the CAST experiment

CAST finished Phase I (in which, the axion mass up to 0.02 eV was scanned), in 2004, and started Phase II in 2005 (in which, the range scanned for the axion mass will be extended to 0.8 eV). In Phase I, there was only vacuum inside the magnet bores, where the axion conversion is expected to take place. In Phase II the conversion

[2]The lower limit for the vertical angle was further reduced to -6.8^o during Phase1 - see section 5.1 for more details.

medium is helium. This in effect would increase the refractive index, hence slow down the photons in order to satisfy the coherence condition for higher axion masses (more on this later in Section 2.2).

1.3. The Dark Matter and the Axion Particle

We can observe only 4% of all the matter in the the universe. The rest, is made of dark matter and dark energy. What we will be focusing on will be the dark matter that supposedly makes up 22% of the universe.

While dark matter can further be classified, in two categories, cold and hot dark matter, the main principle stays the same: we cannot observe it. Cold dark matter corresponds to the primordial low energy dark matter which forms the galactic halos,[3] while hot dark matter corresponds to the high energy dark matter which is continuously produced, in the sun, in the galactic center, or anywhere else that is able to provide enough energy for the production.

There are several particles being suggested for the dark matter. The two outstanding candidates are the axions and WIMPs (Weakly Interacting Massive Particles). While in many interesting experiments WIMPs are also searched for, what we will be focusing on is the axion particle. Axion is a hypothetical particle which was proposed as a solution of the "Strong CP Problem" [4]. Later on, as it became a prime Dark Matter candidate, it gained importance. Currently, aside from CAST, there are several other experiments looking for the axion, all in different regions in the coupling constant-axion mass parameter space (Figure 1.3), mostly because of the intrinsic differences in the natures of these experiments. CAST is the last among a line of similar experiments and has the largest efficiency compared to the previous experiments such as Tokyo Axion Helioscope [5], SOLAX [6] or COSME [7]. There are other kinds of axion search experiments like PVLAS [8] or ADMX [9]. PVLAS searches for ellipticity acquired by a linearly polarised laser beam after passing through a vacuum region with high magnetic field, and ADMX searches for halo axions [10] through a microwave

[3]The galactic halo of the Milky Way contributes most of the mass in our galaxy.

resonant cavity. On the other hand, CAST and the aforementioned experiments try to observe the axions coming from the sun, by converting them into x-ray photons through a strong magnetic field, with Primakoff effect.

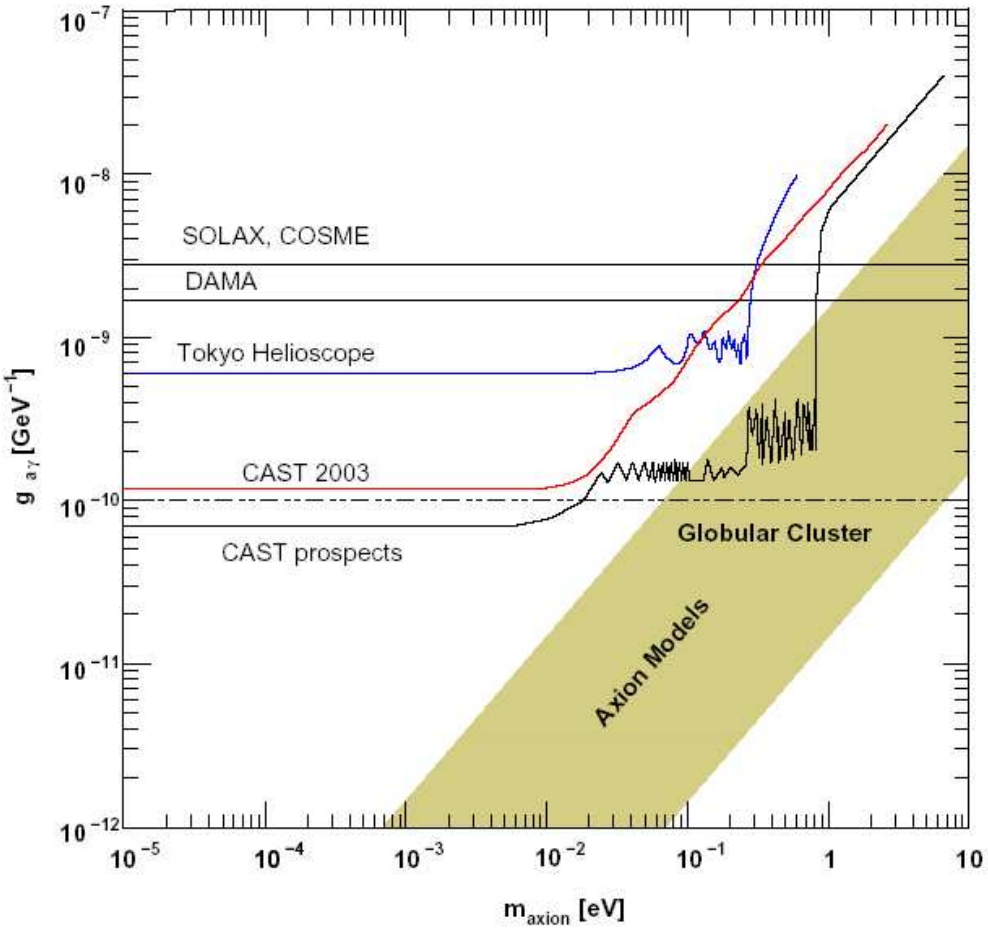

Figure 1.3. The exclusion plot of coupling constant vs. axion mass. In this diagram, it can be seen how CAST will push the theoretical limits for the axion

There are many theories that are bases for the different experiments, each searching for a different axion signal. The common point of all of these theories is however, that the axion should be a neutral, spin-parity 0, very light particle that has a very small coupling constant.

One of the theories suggest that the photons travelling in the interstellar magnetic

fields may oscillate into axions. In case of the distant supernovae, this might produce an effect which will dim the light coming in [11]. This is even suggested as an alternative to the accelerating universe theory for explaining supernova observations.

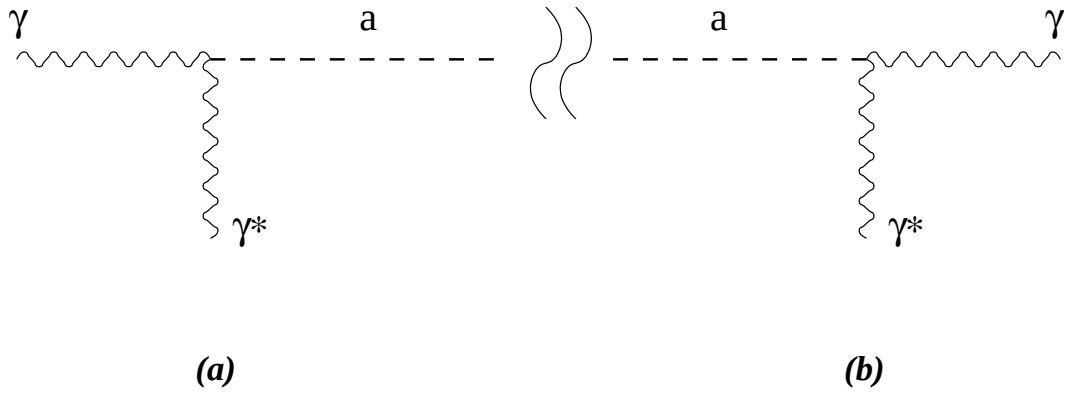

Figure 1.4. a) In the sun, an x-ray photon interacts with the electromagnetic field via the Primakoff effect. b) In the magnet, an axion interacts with the magnetic field to produce an x-ray photon

While some of these theories suggest axions to be remnants of the Big Bang, forming the galactic halos, some other theories state that the axions might be produced in the stellar interiors via Primakoff effect [12]. The Primakoff effect is the scattering of a photon off the magnetic field to produce an axion (Figure 1.4a). This process can be reversed as well, allowing us to "observe" the axions in laboratory (Figure 1.4b), as the x-ray photons produced by the conversion of axions through the high magnetic field are detected. As such,the sun becomes a perfect source of axions for most of these experiments.

The calculations show that the axion production in the sun should be taking place near the core; the axions having both an increased luminosity and increased energy as the depth that they were produced increase.

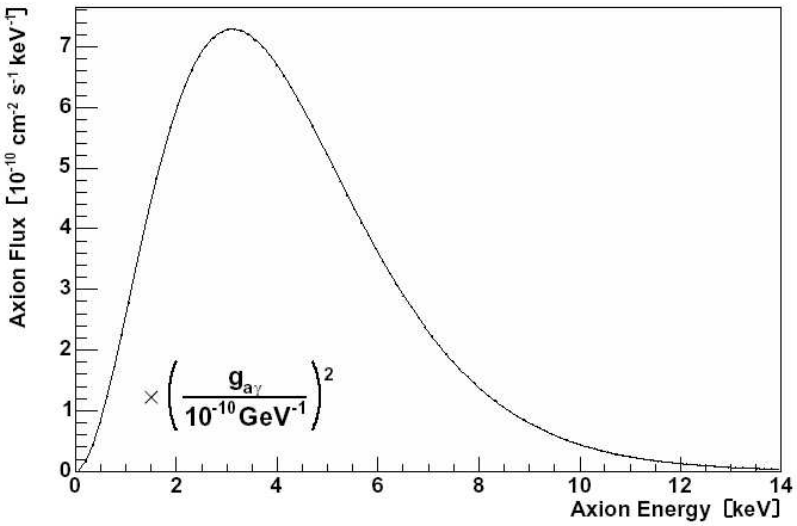

Figure 1.5. The theoretical axion flux on earth depending on the energy of the incoming axions

Calculations [13] originating from the same model [14] reveals that the axion flux at earth should peak at about 2-7 keV (Figure 1.5). Therefore the detectors of the CAST experiment search the axion in about one order of magnitude range around these values.

One other theory about axions being produced in the sun makes use of the observation of the sun's corona, and the reduced x-ray observations. The reduced number of photons coming from the sun's corona were a cause of debate, and this theory suggests that some of the photons might be converted into axions in the magnetic fields above the sunspots, causing this reduction in the photon flux [15].

If the CAST experiment observes the axion signal, this will not only prove the existence of the axions, but also that they are produced in the sun by Primakoff effect, escape the sun's magnetic field before converting back, and that they can be detected by converting them back again through the Primakoff effect. On the other hand even if CAST is not successful in finding the axion, it will introduce the best limit on the

mass of the axions so far.

This work was produced just before and during the start of Phase II, denoting some of the specific problems and aspects of the experiment which arose during that critical transition period.

2. THEORY

2.1. Strong CP Problem

The QCD Lagrangian has a non-perturbative term aside from the perturbative part:

$$\mathcal{L}_{QCD} = \mathcal{L}_{pert.} + \overline{\theta}\frac{g_s^2}{32\pi^2}F^{a\mu\nu}\tilde{F}^a_{\mu\nu} \tag{2.1}$$

where g_s is $\sqrt{4\pi\alpha_s}$, and α_s is the strong coupling constant. $\overline{\theta}$ is given by,

$$\overline{\theta} = \theta + Arg det\mathcal{M}, \tag{2.2}$$

where $\mathcal{M}$ is the quark mass matrix. Note that $\overline{\theta}$ is composed of two parts: θ is the coefficient of the bare $F\tilde{F}$ term in the Lagrangian whereas Argdet $\mathcal{M}$ comes from quark mixing. $F^{a\mu\nu}$ is the gluon gauge field strength tensor (see Appendix A),

$$F^{\mu\nu} = \begin{pmatrix} 0 & E^a_x & E^a_y & E^a_z \\ -E^a_x & 0 & B^a_z & -B^a_y \\ -E^a_y & -B^a_z & 0 & B^a_x \\ -E^a_z & B^a_y & -B^a_x & 0 \end{pmatrix}, \tag{2.3}$$

The $\overline{\theta}$ factor in Equation (2.1) implies violation of CP symmetry which is never observed experimentally. The experiments on the neutron dipole moments showed that $\overline{\theta} < 10^{-10}$. This requires a fine tuning between the two contributions to $\overline{\theta}$ so that they cancel. The reason for this phenomena could naturally be explained by the Peccei-Quinn mechanism [4].

According to this solution, going back to the $\mathcal{L}_{QCD}$; one must first replace $\overline{\theta}$ by,

$$\overline{\theta} \rightarrow \left(\overline{\theta} - \frac{\phi_A}{f_A}\right), \tag{2.4}$$

to resolve the CP problem. This is basically changing an arbitrary parameter to a dynamic variable with a classical potential minimized by $\overline{\theta} = 0$ In this case, the non-perturbative term in the Lagrangian becomes,

$$\mathcal{L} = \left(\overline{\theta} - \frac{\phi_A}{f_A}\right) \frac{g_s^2}{32\pi^2} F^{a\mu\nu} \tilde{F}^a_{\mu\nu} \tag{2.5}$$

$$= \left(\overline{\theta} - \frac{\phi_A}{f_A}\right) \frac{\alpha_s}{8\pi} F^{a\mu\nu} \tilde{F}^a_{\mu\nu} \tag{2.6}$$

Also, we see that the $F^{a\mu\nu}\tilde{F}^a_{\mu\nu}$ factor is nothing other than the dot product:

$$F^{a\mu\nu}\tilde{F}^a_{\mu\nu} = 4\vec{E} \cdot \vec{B}, \tag{2.7}$$

since, to obtain $\tilde{F}^a_{\mu\nu}$ one only has to change the places of E→B and B→-E within the gluon gauge field strength tensor. So, what we have as the non-perturbative term in the Lagrangian is,

$$\mathcal{L} = \left(\overline{\theta} - \frac{\phi_A}{f_A}\right) \frac{\alpha_s}{8\pi} \vec{E} \cdot \vec{B}. \tag{2.8}$$

On the other hand, this solution also proposes another particle, called the axion with a theoretical mass,

$$m_{PQ} = 6\,\mathrm{eV} \frac{10^6}{f_{PQ}/1\,\mathrm{GeV}}. \tag{2.9}$$

The coupling of this particle to the standard model particles can be seen to be inversely proportional to f_{PQ}. The global symmetry proposed as the Peccei-Quinn symmetry spontaneously breaks at this scale, which solves the strong CP problem. Axion is the associated particle with this symmetry breaking.

2.2. Axion Conversion and Coherence Condition

As was introduced earlier in the introduction, the Primakoff Effect is responsible for the production of axions within the core of the sun. We also try to use the same

mechanism in the CAST experiment to convert the axions coming from the sun back into x-rays. For this, we need a high magnetic field, and just the right length of conversion space. Too long a distance might cause us to lose coherence (as we shall see) and too short a distance might not give enough statistics, since the conversion probability is directly proportional to the square of the length L,

$$P_{a\to\gamma} = \left(\frac{Bg_{a\gamma}}{2}\right)^2 L^2 \frac{sin^2(qL/2)}{(qL/2)^2} \tag{2.10}$$

where $g_{a\gamma}$ is the axion-photon coupling constant and,

$$q \equiv p_\gamma - p_a \tag{2.11}$$

in which p_γ is the photon momentum, and p_a is the axion momentum. The mass energy relation states that[4] ,

$$\begin{aligned} p_a^2 &= \omega^2 - m_a^2 && (2.12)\\ p_a^2 &= \omega^2\left(1 - \frac{m_a^2}{\omega^2}\right) && (2.13)\\ p_a &\cong \omega\left(1 - \frac{m_a^2}{2\omega^2}\right) && (2.14)\\ \omega - p_a &\cong \frac{m_a^2}{2\omega} && (2.15) \end{aligned}$$

Since the photon momentum and the photon energy are the same in vacuum, $p_\gamma = \omega$, we obtain,

$$q = p_\gamma - p_a = \frac{m_a^2}{2\omega}. \tag{2.16}$$

The coherence condition states that in order to maximize conversion probability,

[4]In our formulae, natural units were used, i.e. $\hbar = c = 1$.

the phase difference between the axion and photon waves has to have a limit:

$$qL < \pi \tag{2.17}$$

which means that the difference between the two momenta, (i.e. of the photon and of the axion) times the length of the conversion region must be less than π. However, one should keep in mind that Equation (2.16) is valid only when the conversion region is vacuum. When we have some medium with a refractive index within the bore, we can only say,

$$q = p_\gamma - p_a \tag{2.18}$$

$$= p_\gamma - \sqrt{\omega^2 - m_a^2}, \tag{2.19}$$

so, to scan a higher axion masses while still conserving the coherence, one must increase the refractive index, effectively slowing down the photons. Also, since a specific refractive index is set to make q as close to zero as possible, it is only good for a small range of axion mass. Notice in Figure 2.1 that only a small mass range around 0.03 eV and 0.45 eV has high intensity for the corresponding pressures.

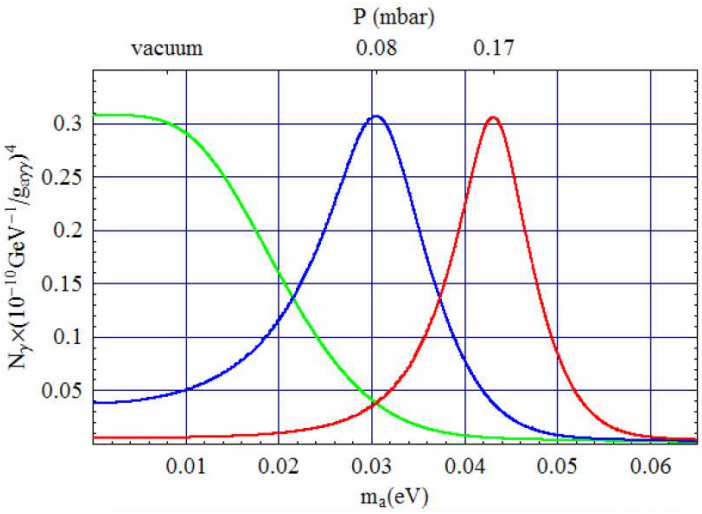

Figure 2.1. The expected signal intensity for vacuum and for ^{4}He pressures of 0.08 mbar and 0.17 mbar, as a function of axion mass

So, how can this coherence factor be important if we are only concerned about

one axion converting into a photon? Why is coherence condition important after the actual conversion takes place? The answers to these kinds of questions lay in quantum physics.

In a double slit experiment, even only one single photon (or any particle - since it also has a wave function) can produce interference pattern if enough single photons are sent through, one by one. This is because even one single photon interferes with itself, since it passes through both of the slits and does not choose one. Just like this, the axion does not convert at a specific point within the conversion region, but it converts in all of the available space at once. This in result, will only produce a photon if all of the different possibilities have the same phase, i.e. the axion and the photon should always be in phase with each other within the conversion region.

On the other hand, the expected number of photons in the detectors depend on several factors like the bore area, exposure time, conversion probability, and of course the actual incoming flux. We can say that,

$$N_\gamma = \int \frac{d\phi_a}{dE_a} P_{a\to\gamma}\, S\, t\, dE_a \tag{2.20}$$

where N_γ is the total number of photons, $P_{a\to\gamma}$ is the conversion probability, S is the magnet bore area (14.5 cm^2), and t is the exposure time.

Putting the values of B and L for CAST experiment (9.26 m and 9.0 T) in the conversion probability Equation (2.10) (at perfect coherence) one finds,

$$P_{a\to\gamma} \approx 1.73 \times 10^{-17} \times \left(\frac{g_{a\gamma}}{10^{-10}\mathrm{GeV}^{-1}}\right)^2. \tag{2.21}$$

The axion flux is given by,

$$\phi_a = 3.8 \times 10^{11} cm^{-2} s^{-1} g_{10}^2, \tag{2.22}$$

where g_{10}^2 is simply,

$$g_{10}^2 \equiv \left(\frac{g_{a\gamma}}{10^{-10}\mathrm{GeV}^{-1}}\right)^2, \tag{2.23}$$

the resulting photon flux per day will be,

$$\phi_\gamma = \left(0.51\,\mathrm{cm}^{-2}\mathrm{d}^{-1}\right) g_{10}^4 \left(\frac{L}{9.26\,\mathrm{m}}\right)\left(\frac{B}{9.0\,\mathrm{T}}\right). \tag{2.24}$$

Thus, if the $g_{a\gamma}$ is taken to be 10^{-10} GeV^{-1} and the bore area of 14.5 cm^2 is used, the expected number of axion photons in each bore per day would be,

$$N_\gamma = \Phi_a\, A\, P_{a\to\gamma} = 7\ \mathrm{d}^{-1}. \tag{2.25}$$

After the gas is introduced into the cold bore, another factor also comes into the play: the absorbtion coefficient, Γ. The probability of conversion then becomes,

$$P_{a\to\gamma} = \left(\frac{Bg_{a\gamma}}{2}\right)^2 \frac{1}{q^2+\Gamma^2/4}\left[1+e^{-\Gamma L}-2e^{-\Gamma L/2}cos(qL)\right], \tag{2.26}$$

where q is the momentum transfer,

$$q = \left|\frac{m_a^2-m_\gamma^2}{2\omega}\right|, \tag{2.27}$$

and the coherence condition, $qL < \pi$ is satisfied.

3. THE EXPERIMENT

As stated before, the CAST experiment started in 1999. The 20 ton magnet is supported by a similarly massive frame, and all the structure is supported on one side by a 'pylon' and on the other side by two support beams with adjustable lengths. The whole structure can also be rotated in the horizontal plane. Of course, angle encoders are installed to ensure the precision of the magnet movement, since the whole purpose is tracking the sun, and even one degree error is enough to doom the experiment (more on this in Chapter 5).

For the high magnetic field, superconductivity has to be achieved within the magnet coils, so that a current in the order of 10 kA does not produce a problem. To have superconductivity a very low temperature is required. This is only possible by using liquid helium refrigeration. Also, since the magnet is operated at the maximum current to obtain the highest magnetic field possible, having a quench (see Section 4.2.1 for details on quench) is much more likely than the magnets used in LHC. To prevent this as much as possible, a whole group of cryogenics people is assigned to the magnet (more on this in Section 4.2).

During Phase I, the interior of the cold bore was vacuum. In Phase II however, the interior is filled with ^{4}He, with variable low pressure. This would allow different mass ranges for the axion to be scanned. For the precise pressure control, an ingeneous pressure system was installed before the beginning of Phase II (more on this in Section 4.3).

The pressures inside the different magnet regions are very important, both to prevent quenches and to have a precise ^{4}He density measurement. For these reasons a number of pressure and temperature sensors are installed within the magnet and the cold bore. Monitoring these sensors, and recording the measurements are entrusted to a single system, whose sole responsibility is monitoring and controlling of the alarms (more on this in Section 5.3).

Each detector has its own sub-group of people to handle problems. They all have online and offline analysis programs which can be used to check if the data is being correctly taken and to analyze the data respectively. A shift person is responsible to know how to use the online analysis program, in case something goes wrong (more on this in Chapter 7).

3.1. Basic Conventions

As with every experiment, certain subjects specialized for CAST has to be named, in order to facilitate understanding among the members of the collaboration. In order to achieve this, certain coordinates, even basic directions like left and right had to be renamed. Of course, for some concepts which are unique to CAST, names had to be invented.

Since the magnet of CAST is not stationary, the meaning of left and right are vague at best, depending on the observers point of view, much like on a ship, so just like on a ship, the two sides of the magnet are renamed. While this seems to have happened unconsciously, the names seem to have stuck. While looking from the side that has the MicroMEGAS and CCD detectors towards the TPC side, on the right there is the airport, and on the left there is Mount Jura (and since the magnet cannot sweep an angle more than 180^o, the sides are more or less always correct), so these sides are named as such, Airport and Jura.

There is another directional problem however. The CAST experiment does not have a specific direction that can be called front or back, since at different times, the magnet is oriented so that different sides face the sun. To get rid of this problem, the sides can also be called by the names of the detectors that are stationed there. Conventionally, the CCD and the MicroMEGAS side is called MFB[5] and the TPC side is called MRB.[6]

[5]Magnet Feed Box, the entry point for all the cryogenics and the current.
[6]Magnet Return Box, the return point for the cryogenics and the current.

One other problem is defining the angles, which the magnet is pointing at. Of course, defining the difference on angles is not a problem, but defining the "zero" might be. So, the start of the rails[7] at the Jura side is set as "0" and with the help of an encoder system (more on this in Section 5.2) the azimuthal angle of the magnet is defined by how much the current encoder value differs from zero. The vertical angle, on the other hand, has a zero at the lowest point, and similarly increases as the TPC side is elevated.

The two bores within the magnet are called by the names of the detectors attached to them at the MFB side, since TPC covers both bores. So, CCD and MicroMEGAS bores also contain the cold windows, valves and everything else that can be called by the same names.

On the other hand, especially valves, but also other safety measures, pumps, sensors must have specific names, not dependent on their direction or where they are stationed, so that in case something goes wrong, there will not be any pause to think of the conventions. So, every pump, every valve, every sensor has a specific name (actually a code, like VT2 or P4VA). The information on specific names of these components can be found in their relevant chapters and in Appendix B for a complete listing.

[7]The horizontal movement of the magnet is via wheels moving on rails

4. CRYOGENICS AND THE SUPERCONDUCTING MAGNET

The magnet used for the CAST experiment is a decommissioned prototype LHC magnet, as stated before. Thus, it has almost the same characteristics of an LHC magnet, despite being a little shorter.[8] The cross-section of the magnet can be seen in Figure 4.1 in detail.

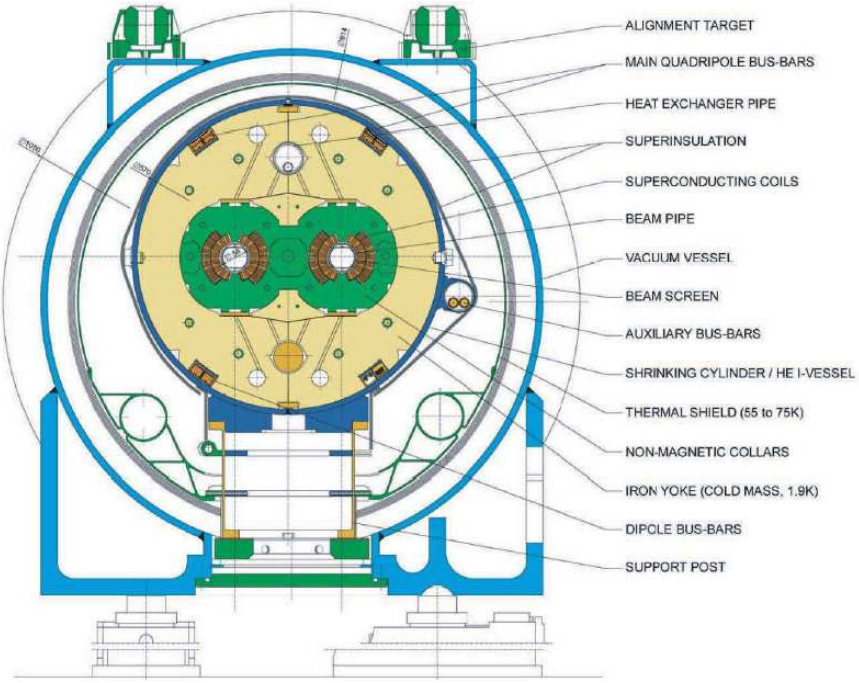

Figure 4.1. The cross-section of the CAST Magnet

4.1. Current Supply for the Magnet

The magnet of CAST produces a 9 T magnetic field in order to have efficient axoin-photon conversion. However this can only be achieved by having a very large current passing through the superconductors. The answer to the question of "how large?" to be exact is 13000 A. Obviously this is not something to be taken lightly.

[8]While the LHC magnets are 15 m in length, the magnet of CAST is only 9.3 m.

The current is supplied to the magnet by heavy cables surrounded by water. The water helps to prevent overheating while the sheer number and thickness of the wires can withstand the current itself. The whole setup is hung about 5 m high, connecting the cables to the magnet. The name given to this movable setup is “potance”.

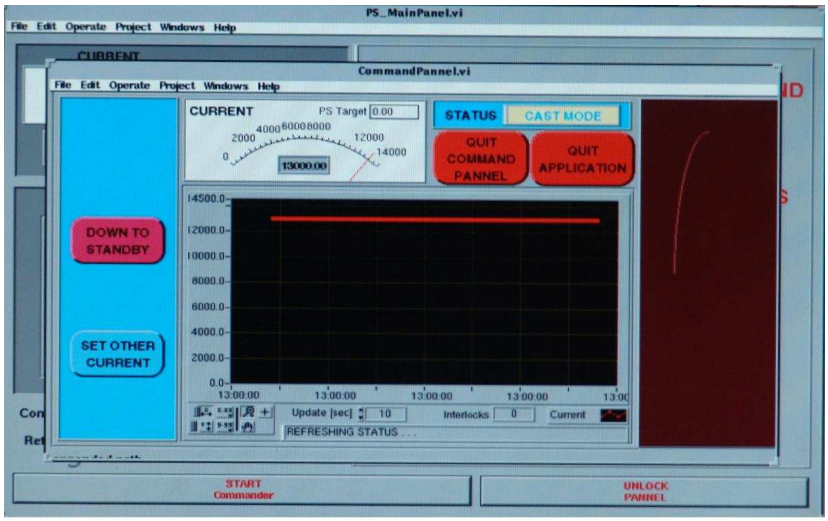

Figure 4.2. The current control program located in the control room

While the stable working conditions for the magnet with 13 kA might be perfectly fine, it is not that easy to ramp the current up or down. The change in the current produces inductive effects which result in extra heating. To prevent this extra heating, the current has to be ramped up (or down) gradually. This would give the cryogenics time to cool. While this may easily be done manually, a labview program was designed, because not all of the shift people might be as careful, or know as much as the experts.

What the program does, is basically ramp up (and down) the current in steps, to a given current. It also prevents shutting the current down at once and not only it graphically shows the set current at that moment but also it shows the history of the current (Figure 4.2).

4.2. Cryogenics

The currents that maintain the magnetic field of 9 T in the CAST magnet are much too high to be contained in ordinary wires. Instead, superconductors have to

be used, and for superconductivity, one needs extremely low temperatures. For this reason a relatively new science, cryogenics is used. The magnet is kept near absolute zero during operation, so that the resistance of the cabling is reduced to zero, and the high magnetic field can be maintained through the high current value reached.

The cryogenics requirements of CAST are provided by an expert team of CERN via the cold box stationed near the magnet. The temperature of the cold bore is kept at 1.8 K, and is constantly monitored. Of course, in some cases, this temperature can go up and this can produce undesired effects, like the quench.

4.2.1. Quench

Quench is the term used for the failing of cryogenics and exhaust of the He that changes into the gas phase with the temperature increase. There might be several reasons for a quench, while the triggering by an actual temperature increase is quite rare. For example, of the eight quenches that were reported between 10^{th} of July to 14^{th} of November 2005, four were caused by perturbations in the electrical network or thunderstorms, one was caused by the disconnection of a monitoring PC from the magnet power supply, one was caused by a CAST operator issuing an off command, one was caused by a false alarm signal from the cryogenics resulting in a fast ramp down, and only one was caused by a real temperature increase during a ramp up.

While CAST uses an LHC magnet and LHC itself has many more of these magnets, CAST has much more quenches than the LHC.[9] This might seem weird at first look, but one has to keep in mind that CAST uses the very maximum current that the magnet can use, as a result, it is always at the border of operation range. On the other hand, LHC uses only about half of their maximum current value.[10] When there is a quench trigger, the He boils with an avalanche effect. As a result, a high pressure gas is trapped within the magnet and this gas is let out from the safety valves. Immediately

[9] What is more, if one of the magnets in the LHC undergoes a quench, all the others also will, in an avalanche effect.

[10] The 1232 dipole magnets of the LHC operate at about 5 kA giving a magnetic field about 8.34 T [16] but one must also keep in mind that the magnet of CAST is only a prototype, not a replica of the LHC magnets, when comparing the current and the magnetic fields.

after the quench the magnet has to be moved to a parallel position so that no gas is trapped within, when the recooling procedure is started.

4.3. The Cold Bore

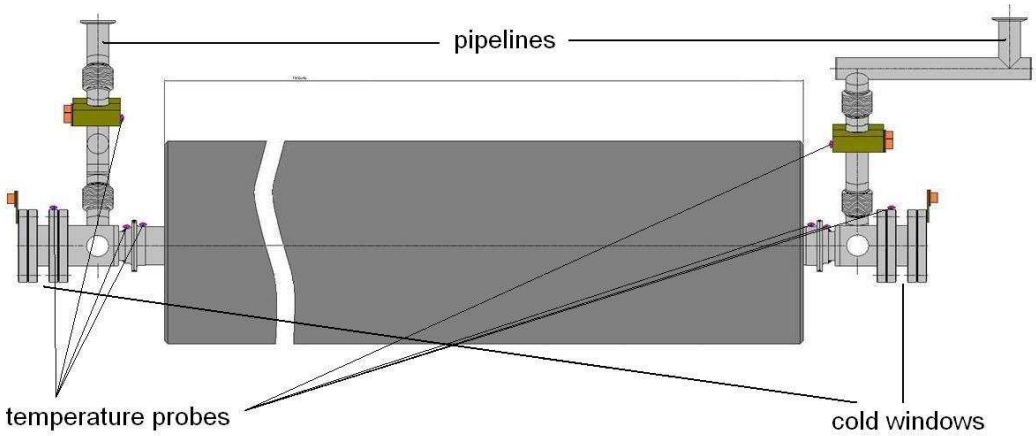

Figure 4.3. The layout of the cold bore

The cold bore is basically the inside of the magnet, where the axions transform into photons, and where the ^{4}He for Phase II is kept. Figure 4.3 shows the layout of the cold bore inside the magnet showing the cold windows, the temperature probes and the pipelines which the pumping system and the ^{4}He system is using for gas input/output. It is kept at 1.8 K during the time the current is up, which means through the data taking period. The ^{4}He is confined between the cold windows within the cold bore and the pressure can be increased very precisely.[11] The cold windows are made of polyproplene[12] and are mounted on a strongback to withstand the pressure differences, especially during a quench. One other requirement is that the cold windows must have a very low leak rate (the current windows have less than 10^{-8} mbar/sec at 1.8 K) because one side is vacuum while the other side is ^{4} with a very precisely defined pressure.

[11] The precision of this system is more than 0.01 mbar as we shall see in the pressure settings section.

[12] The material for the cold windows have been tested in the Panther testing facility in Germany for transmission and polyproplene was found out to be the best material.

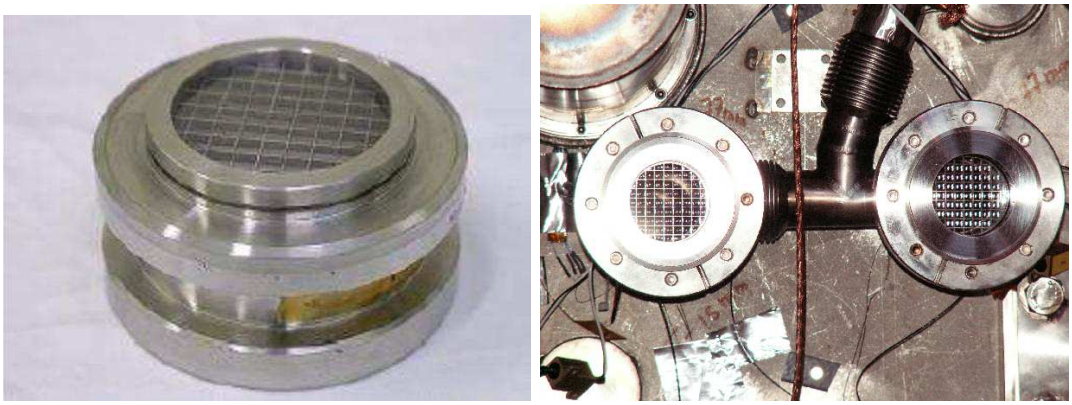

Figure 4.4. The cold windows, outside of the magnet and mounted on the cold bore. The gas input/output lines can also be seen in the right picture

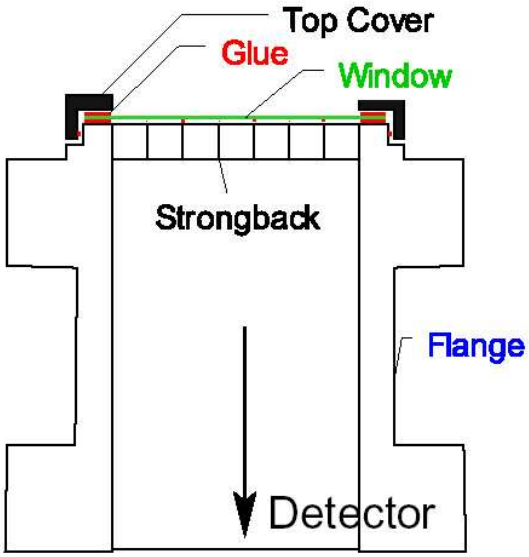

Figure 4.5. The schematic diagram of the windows

In the testing facility, 4, 12, 23 μm of polyproplene and Al coated 12 μm of mylar have been tested as window materials. The strongback is electro-eroded material having 5.2×5.2 mm^2 cell size and 89% transmission. The glue that is connecting the window to the frame is Araldite 2018, which is basically polyurethane (Figure 4.5) [17].

4.3.1. Thermo-Acustic Oscillations

After the cold windows were inserted and the first ^{4}He was put into the cold bore, pressure readings were made in order to make sure nothing is out of order. The problem arose when it was realized that different sensors observe different pressures and all of them were showing oscillations. It was then realized that there were thermo-acoustic oscillations within the cold bore, just like a standing sound wave.

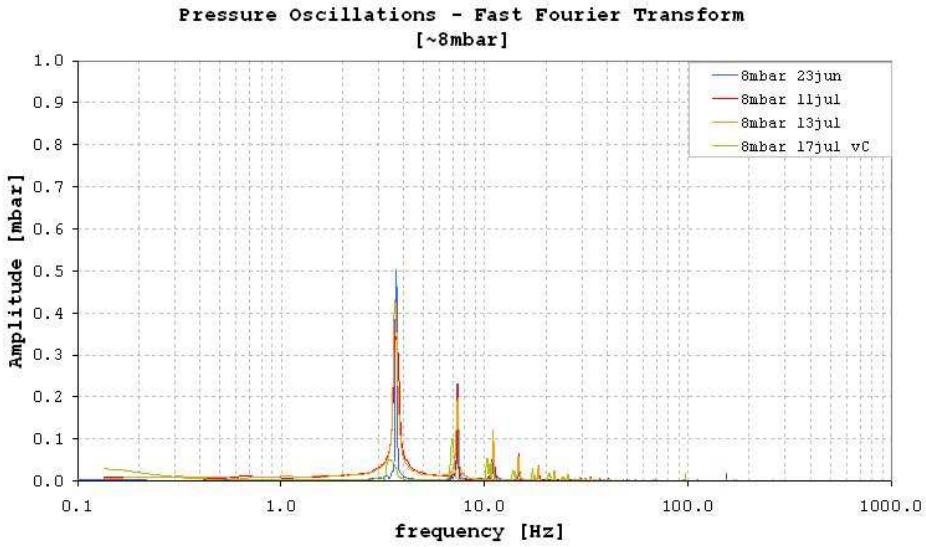

Figure 4.6. FFT (Fast Fourier Transform) of the Thermo-Acoustic Oscillations. Amplitude in mbar vs. frequency

FFT (Fast Fourier Transform) analysis showed resonance frequencies at integer multiples of 3.7 Hz (Figure 4.6). After much experimenting and calculations, a way to dampen these oscillations was devised. Basically, since it was thought that the oscillations might be caused by the pipelines being considerably hotter than the cold bore, and the transfer of the gas from the pipelines to the cold bore and vice versa can be causing these oscillations within the cold bore, the theory was to install something in the pumping lines which would prevent the gas flow somewhat. So, the dampers were installed and the resulting pressure readings indeed showed that the oscillations

were damped considerably, down to almost negligable levels (Figure 4.7).

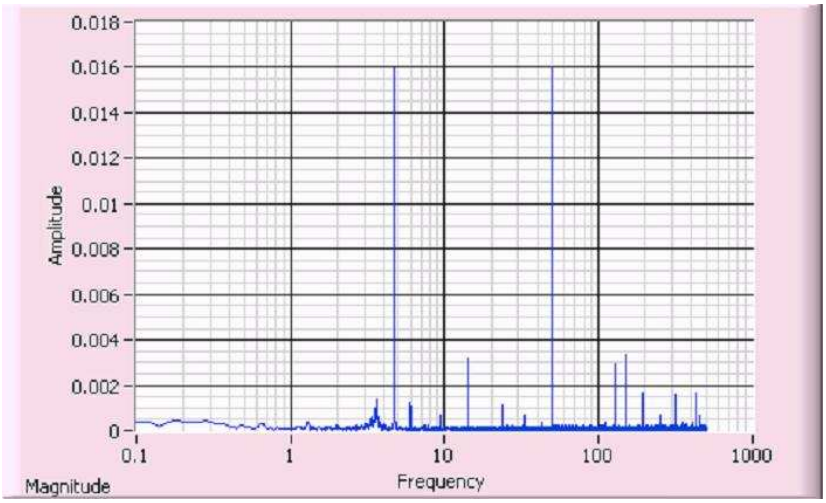

Figure 4.7. What is remaining from the Thermo-Acoustic Oscillations. The peaks that can be seen are only because of electronic interference on the sensors, not related to the Thermo Acoustic oscillations

4.3.2. Cold Window Spots

After the ^{4}He was introduced to the cold bore and the temperature of the cold bore is dropped to 1.8 K, it was observed that some dark spots appeared on the cold windows (Figure 4.8). It was feared that these spots might be caused by an oil leak from one of the vacuum pumps; if they were, cleaning the leak and preventing it from happening again would prove to be quite a hard task. Hence, to find the real cause, try to eliminate it, and if not successful in removing the spots, at least determine if they present a danger to the well being of the experiment, a series of sub-experiments were conducted for different possible causes.

4.3.2.1. Diffraction Effects. One possible cause for such spots could be an effect of diffraction. To test this hypothesis, an optical bench was set up with a theodolite, four spare windows (two with polyproplene foil, two without), and a white light source.

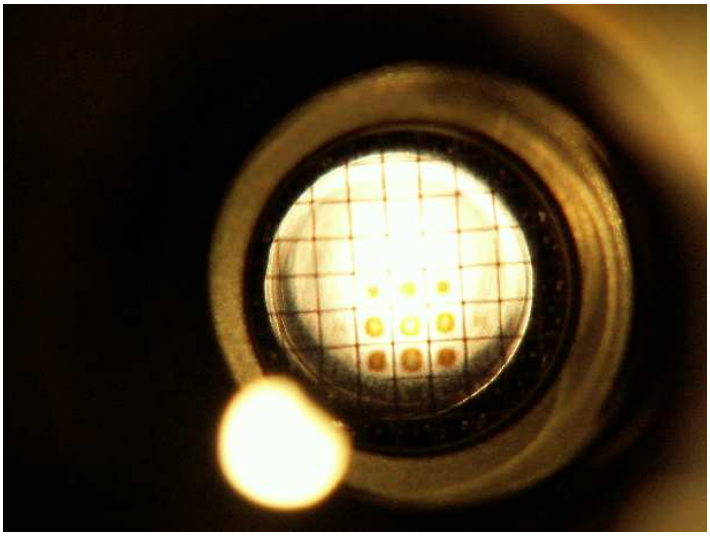

Figure 4.8. The spots on one of the four cold windows illuminated from behind as seen from the TPC side

Various trials, aligning two of the four windows with the parallel laser beam, produced no results. The white light source similarly didn't produce any result either.

4.3.2.2. Reflection Effects. Another possible cause could have been the reflection of the cold bore itself. To test this, a pipe which has a similar diameter to the cold bore, and which had reflective inner surface was inserted between the two windows, before the first window and the combinations of these orientations. Similarly, no effect resembling the effect in the cold bore was observed, either with the laser or the white light.

4.3.2.3. Lens Effect. The pressures inside the cold bore on the two sides of the cold windows are different, and since the foil on the windows is flexible material, it stretches. The resulting effect might have been focusing of the light by the ^{4}He between the two cold windows, which might act as a lens when the foil streches outward between the openings of the strongback beacuse of the pressure difference. However, a quick analysis immediately disproves this hypothesis also, since the spots are not homogenously distributed between the openings. Also, the foil itself might have acted as a lens when it was streched. This hypothesis was also dismissed, since any effect the foil might have

had would be very small beacuse of its very small thickness ($\sim$ few μm).

4.3.2.4. Precipitation Effect. One other source that can cause this kind of spots could have been the condensation of gasses on the foil of the cold windows, when the cold bore temperature was lowered. The vapor present within the cold bore would have condensed into liquid or solid (depending on the material). For example H_2O would solidify on the cold windows. Calculation shows that an H_2O layer of $\sim$1 μm concentrated at the center of the cold window openings (Figure 4.9) would produce similar spots to Newton's Rings.

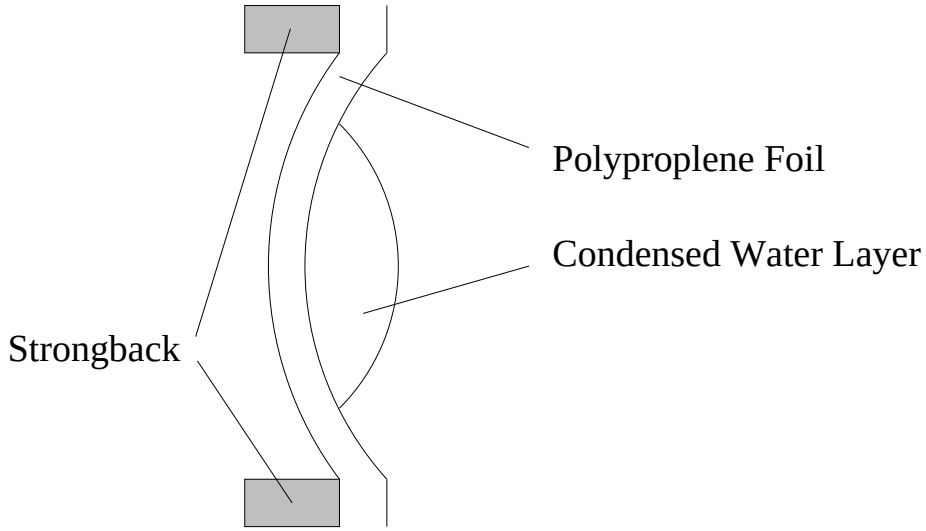

Figure 4.9. The H_2O is thought to be filling the concavity produced by the pressure difference between the two sides of the cold window and the strongback

4.3.2.5. The Physics Behind. The phenomenon known as Newton's Rings is usually associated with a lens resting on a glass surface horizontally, therefore producing a ledge of air between the two surfaces. The glasses at either side of the air act as reflectors, and since their refractive index is greater than that of air, the reflections result in a half wavelength phase difference in the reflected wave. Therefore the reflected light is observed to have destructive interference, while the transmitted light has constructive interference behavior at the center, where the optical path difference is practically zero compared to the wavelength.

On the other hand, in our case the situation is a little different. First of all, the medium of the thin ledge is water. Next, it is thickest in the center and the one of the surrounding media is polyproplene while the other is low density ^{4}He. This causes a number of phenomena different from the classical Newton's Rings.

The refractive index of polypropylene is 1.45, which is higher that of water, 1.33. This causes the reflections from polypropylene to be similar to the textbook example, with a change in the phase by π. On the other hand, the other surrounding medium, ^{4}He has a refractive index near 1.00[13] and this causes the reflection from that side to have no phase shift. Therefore, in the sides, where there is almost zero optical path difference, for the transmission the interference is destructive, while at the center, it totally depends on the thickness of the water film. Since we observe no total rings, and no constructive interference anywhere,[14] we may assume that the thickness of the H_2O film does not exceed quarter of a wavelength, which should be about $\sim$ 0.1 - 0.2 μm, for a wavelength in the visible range. This, of course does not have any relavant effect on x-rays.

4.3.2.6. Solution for the Spots. The appearance of such spots can be actually expected since the temperature of the cold windows was as low as the rest of the cold bore during cooldown. As a result, any gas that would have condensed on the walls of the cold bore would have stuck to the cold windows also. The solution to this problem proved to be an easy one, as there were heaters on the windows. The windows were heated with 10 W power up to 200 K. As a result, the spots disappeared, but the cryogenics could not compete with such heating. Therefore, the power of the heaters were lowered. After the windows reached 120 K and three days past, still no spots appeared. This is probably because during the heating of the windows, all the gas has condensed on the walls of the cold bore, instead of the windows, since the cold bore had definitely a lower temperature. After the detectors were installed, it was not possible to observe the behavior of the spots any further. It was hypothesized that they didn't appear

[13] We can assume this for the purpose of understanding this phenomena. Of course the main purpose of Phase II is changing the density of ^{4}He and hence the refreactive index.

[14] There are spaces on the foil where there is no destructive interference, but this does not suggest constructive interference, it merely suggests that no water had accumulated on the foil on those parts.

again until the break when the detectors were dismounted, however even with taking precautions, the spots have in fact appeared again.

4.3.3. Pressure Settings

The incredible precision of this system is achieved by inserting the gas inside the cold bore in two steps. Firstly, the gas is transferred into a metering volume of 3.5 lt which is kept at 36°C by a temprerature bath. The pressure inside the volume is increased up to 700 mbar. After the pressure fluctuations die out within the metering volume, the gas is gradually transferred to the cold bore. During the data taking period, this process is commenced while the current is at maximum, so extreme caution and patience is neccessary in order not to trigger a quench. The pressure of the metering volume is dropped down to ∼100 mbar[15] and the transfer is finished. Since the temperature of the metering volume is much higher[16] then of the cold bore, the pressure increase in the cold bore is much lower[17] . The result is being able to reach 0.083 mbar pressure steps with a high accuracy. Even a mistake of 10 mbar in reading the pressure of the metering volume with the baratron1000 sensor (accurate up to 10^{-2} mbar) only leads to an error of 1.35×10^{-3} mbar in the cold bore pressure, which is within the acceptable limits.

[15]This value is different for different pressure settings. It is calculated by a program and given to the shift person responsible for the transfer. The difference between the initial and the final pressures is tried to be set to 617 mbar.

[16]Actually, since the cold bore is kept at 1.8 K during operation, the ratio of the two temperatures is about 180.

[17]Again, we have to take the volume of the cold bore into account, which is ∼30 lt while the volume of the smaller metering volume is 0.7 lt.

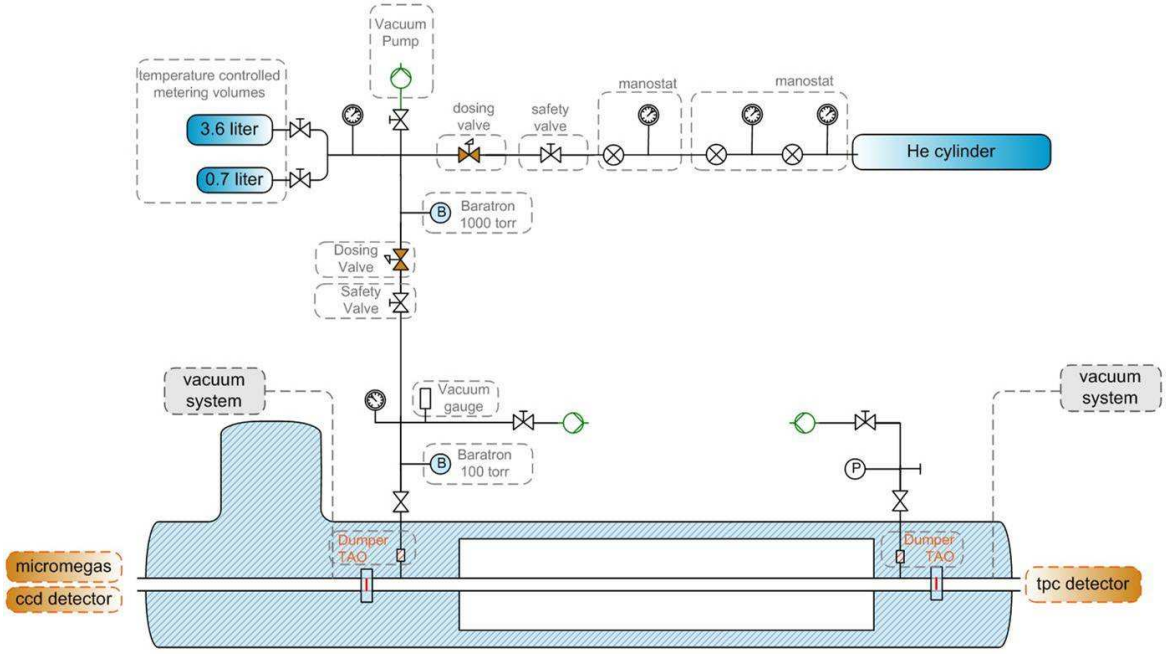

Figure 4.10. Diagram of the gas system showing the positions of the valves, pumps, pressure sensors and metering volumes

5. CONTROL AND FEEDBACK MECHANISMS

As it was stated before, the whole magnet and the support structure weighs about 40 tonnes, and has to be able to track the sun, at least 1.5 hours each morning and each evening. All the movement has to be in harmony with the suns movement, since the whole aim is to point the magnet towards the sun. Every movement has to be double checked, and controlled by the computer and every other possible way.

5.1. Movement and Tracking Control

A PC is dedicated to the movement and tracking control within the control room. The data from the magnet encoders are fed into this computer and the motors are controlled again from this computer for everything except the main circuit breakers, beside the magnet (Figure 5.1). On the other hand, both the vertical and horizontal position of the magnet, the position of the sun and of course, the integration of the two are made by this computer which also uses a program written in Labview.

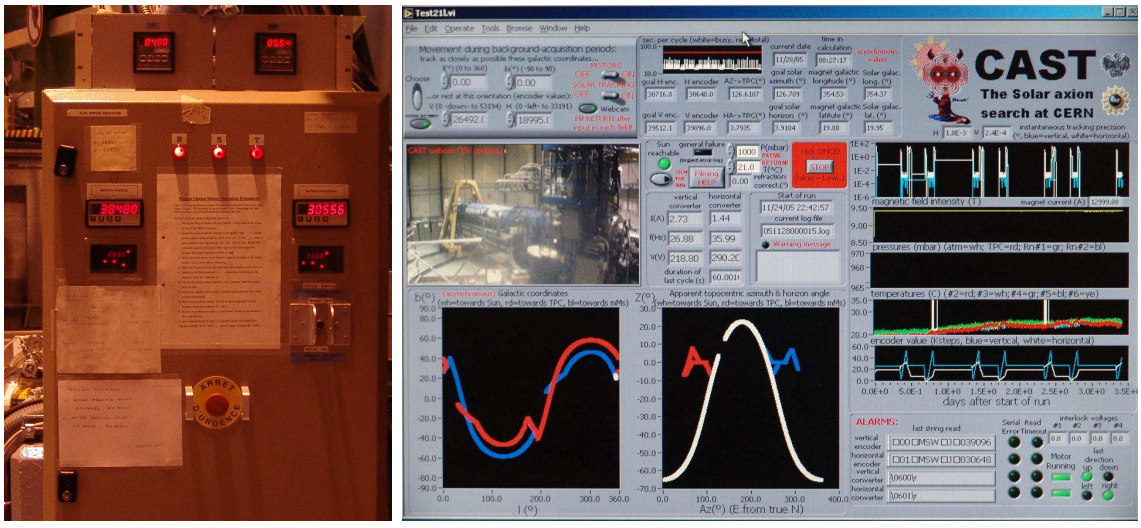

Figure 5.1. *Left:* The manual on/off switches and the circuit breakers together with the displays showing the position of the motors. *Right:* The computer program which calculates the position of the sun, displays the position of the motors, reads the angle encoders, and integrates all the data

There are three motors responsible for making any movement possible at all. Two of them are used for vertical, while one of them is used for horizontal motion (Figure 5.2). The vertical motors are used for changing the length of the support screws that hold the MRB end of the magnet. In 2004, after an accident which fortunately didn't have the direst consequences, safety measures were decided to be installed to the ends of the screws which will prevent the motors from working if the magnet is too low or too high. On the other hand, this resulted in the support beams to be effectively shorter, in turn resulting in the vertical angle sweep capacity to be lowered from $\pm 8.0^o$ to $\pm 6.9^o$.

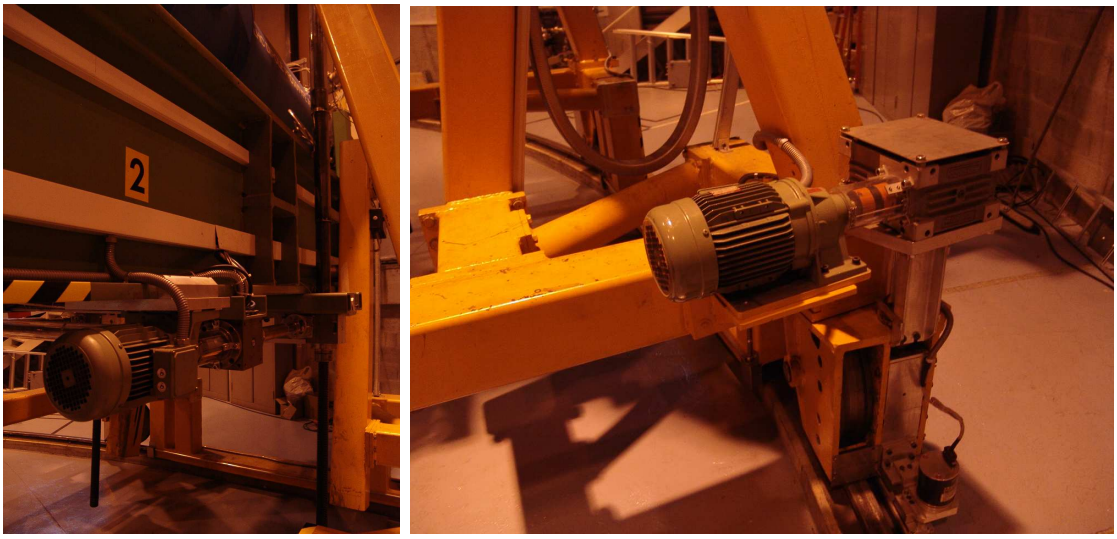

Figure 5.2. *Left*: One of the motors responsible for vertical movement, *Right*: The motor responsible for horizontal movement. The horizontal positioning system can also be seen in this picture

5.2. Encoders

The position of the magnet is not only checked by the positioning system near the motors, but also checked by the angle encoders positioned near the "joint" point (Figure 5.3). These allow double checking of the position, while they are fed to the tracking PC and recorded in the log files, and shift checklists.

To further increase the accuracy of the system, mainly two more methods are used, which are the grid measurements and filming of the sun.

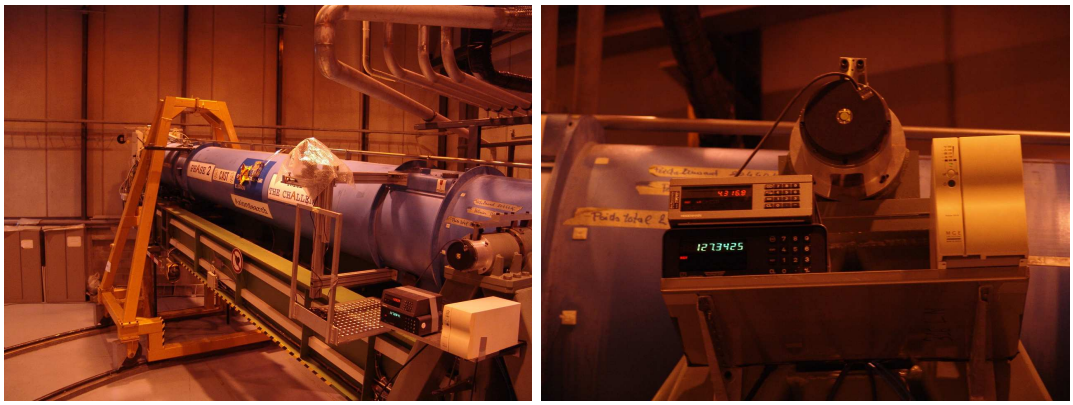

Figure 5.3. The position of the angle encoders with respect to the magnet, and the detail photograph

5.2.1. Grid Measurements

Both the positioning system near the motors and the angle encoders are prone to faliure as they are measuring the position and the angle with respect to the rail on the ground and the pylon. A simple shift in the system might ruin the measurements taken after that point. Therefore, grid measurements are taken periodically by CERN's surveyors.

The procedure for the grid measurements is simply stationing the survey instruments at precise points, positioning reflectors on specific points on the magnet and recording the position of the magnet at specific encoder values. Although the positions at the endpoints of the movable region are essential, they are not enough to safely say that the magnet movement is not problematic. Therefore the magnet is moved to several pre-defined horizontal positions,[18] along the maximum and minimum vertical positions.

5.2.2. Filming the Sun

Of course, the perfect way to check if the magnet is actually looking at the sun or not, is visually seeing the sun through the bores. However there are two problems with

[18]The number of the pre-defined positions are about 100, and the measeurements are also repeated after the magnet is cooled down to working conditions.

this aproach. Firstly, seing the sun at all is a problem within the building that CAST is stationed, and secondly the detectors have to be taken off in order to look through the bore. Fortunately, there is a window through which the sun can be observed during certain periods, twice per year, but only stationing the filming aparatus on the outside of the magnet can bypass the second problem. Therefore, by installing a stationary aparatus on the casing of the magnet, twice per year[19] , we have a means to actually check the sun's position with respect to the tracking system used for magnet alignment (Figure 5.4). The device used is basically a camera looking through a crosshair. The

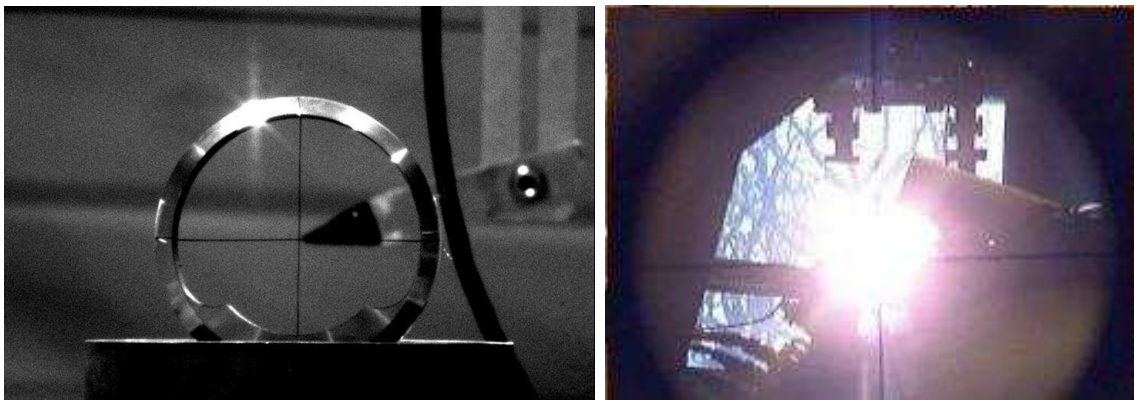

Figure 5.4. The crosshair for the filming aparatus and the sun observed through the window

results are analysed and usually no more than several seconds of angular error is found [18].

5.3. Slow Control

The slow control system, while named so, is actually not a control but a monitoring system. A dedicated PC is used for monitoring the pressures[20] , temperatures and load on the screws that raise and lower the magnet (Figure 5.5).

[19]March and September

[20]Except the pressures and temperatures of the ^{4}He which are controlled by another computer.

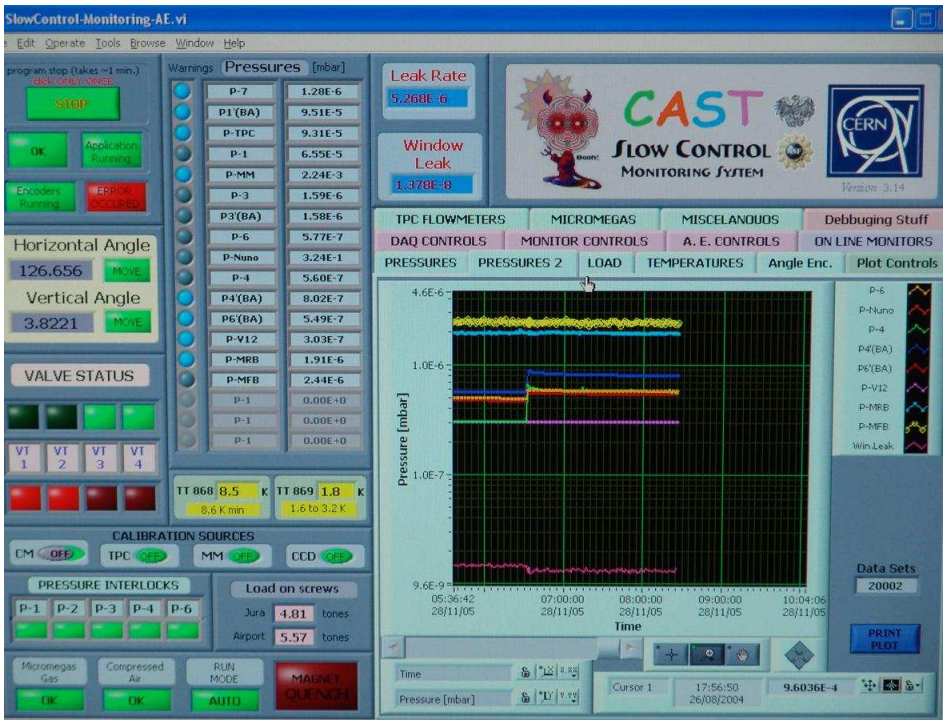

Figure 5.5. The slow control GUI, which shows the temperatures and pressures at various points of the magnet, among other things

The monitoring program is made with the Labview and is a graphical user interface (GUI) which shows all the relevant values on a graph and unless it is reset, it also shows the history of the values. Also, as new pressure and temperature probes are installed, the need to monitor them arises. This results in the slow control program to be constantly upgraded, and constantly updated.

5.4. ^{4}He Monitoring

As with the slow control system, the pressures and temperatures of the ^{4}He is also monitored by a GUI, displayed on another dedicated computer's screen. The ^{4}He monitoring program can also show the history unless it is reset (Figure 5.6).

Figure 5.6. The transient recording program, which monitors the ^{4}He pressure and the temperature, among other things. The picture doesn't show the displayed metering volume pressure, which wasn't implemented at the time of this screenshot

One difference of this program is that it is actually used while inserting the gas into the cold bore, since the process is a delicate process, even if it is manual. This computer is placed outside the control room and the screen is visible from the point where the valves of the ^{4}He system are located. While the gas is being introduced, the value displayed on the secreen for the pressure in the measuring volume must be observed, so that the shift person knows when to stop the gas transfer by checking the pressure from the screen.

6. THE DETECTORS

The most important component in every experiment is the detector which is usually composed of some sub-detectors. Whether it be a human eye or a calorimeter, a spectrometer or a bubble chamber, without the detector to observe, measure, record the results, the experiment has no meaning, no reason for existence. CAST is no exception. From three main sub-detectors in the CAST experiment, one of them covers both bores on one side, and the other two each cover one bore on the other side of the magnet, as stated before. Of course, having three detectors instead of only one which will cover both bores on both sides has a reason: cross checking. If one detector sees a signal when the other two sees nothing, there is something wrong, the detector will be checked, but the others will be checked also. This way, the chances of missing a signal, and the probablity of having errors on the detectors' results is minimized. Of course, this choice (having three different detectors) does produce some problems, like the difficulty of combining the analysis results, or the lowering of the signal/backgound ratio. After all, the least of two evils was chosen.

The specific details are explained for each detector in the following sections, including their geometry, the working principles and the specific tecniques to reduce background. However, the analysis programs will be explained in Chapter 7.

6.1. TPC detector

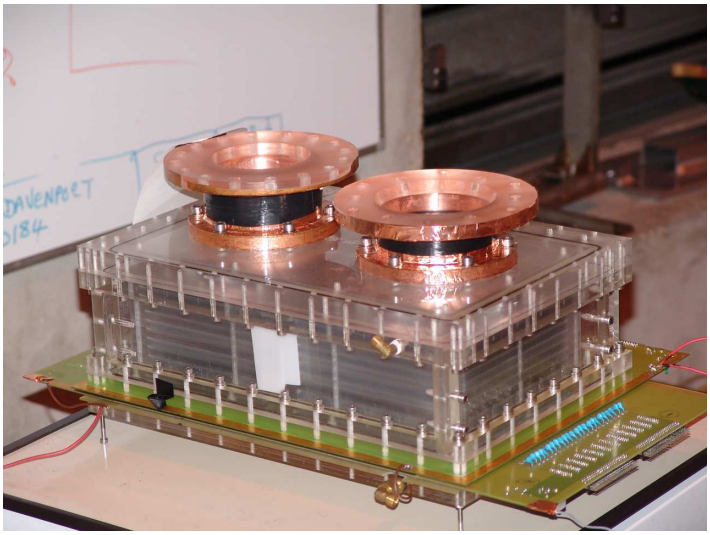

Figure 6.1. The TPC detector of CAST

Also known as the "Time Projection Chamber", the TPC detectors are used extensively, and known to be reliable through many experiments (Figure 6.1), (Figure 6.2).

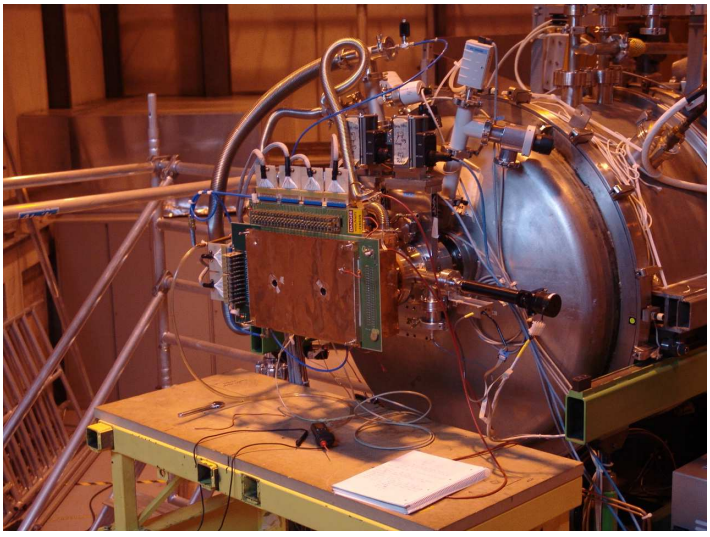

Figure 6.2. The TPC covers both bores, while the other two detectors only cover one bore each

The TPC is basically a drift chamber filled with gas: the high electric field forces electron drift when the atoms of the gas are ionized by incoming radiation. The ionization electrons start an avalanche if the electric field strength is high enough. In the first region, eventhough the potential difference is higher, the electric field is not strong enough to cause a large avalanche effect.

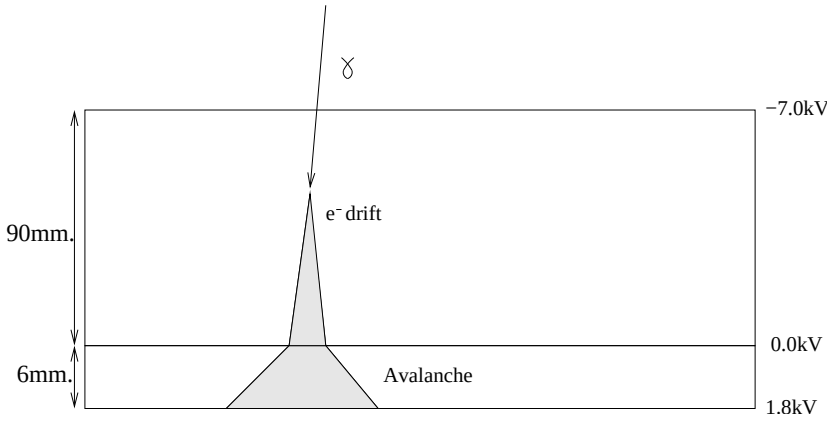

Figure 6.3. The two regions of the TPC detector

On the other hand, in the second region, while the potential difference is much less, the distance over which this potential applied is much more shorter, which produces a larger electric field. This large electric field is enough to produce an observable avalanche even for a small number of ionization electrons (Figure 6.3). As a result, the cone of electrons has an elliptical cross section at the planes defined by the cathode and anode wires. The collection of channels with the pulse amplitudes above the pedestal values (or the collection of the wires that see this cone) make up a cluster, with the highest energy deposition usually near the center of the cluster.

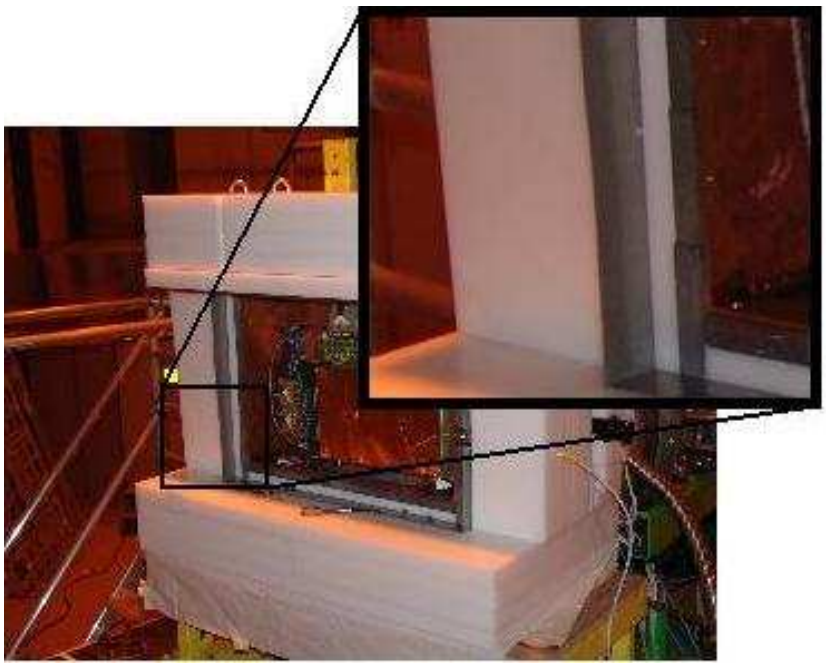

Figure 6.4. The layers of the TPC shielding

Because the TPC has very large background from the surrondings, a heavy shielding was required. Of course, during Phase I, this shielding evolved along with the experiment. The best shielding (that is still used today) was achieved by using a four layer shielding [19] (Figure 6.4). The first, innermost layer is 5 mm copper which acts as a Faraday cage. This layer was installed first, in 2003. Later on, in the beginning of 2004, the other layers, 25 mm lead which shields most of the radioactive gamma background, 225 mm polyethylene which reduces cosmic muons and shields alphas/neutrons, and 1 mm cadmium which acts as a selective filter [20] for the neutron energies below 0.4 eV and as a shield for the inner contamination of lead and for radon intrusion. Also, the interior of the shield is flushed with nitrogen to reduce the radon intrusion. On top of the passive shielding mentioned, a muon veto has also been implemented also. While the distinct muon signals are easily seperated from the x-ray signals, the secondary effects from the muons interacting with the surrounding material (such as the shielding) still produces a sizable background effect [21].

The signal is detected by the cathode and the anode wires on either side of the small gap (with 1.8 kV potential difference across). The anode and the cathode wires are aligned perpendicular to each other, which allows position measurement. The signals from the anode and the cathode wires are read out individually and sent to a dedicated computer in the control room.

The data taken by the detector are sent to the computer in two sets, one for the anode cluster, and one for the cathode cluster.[21] From the sent data, some parameters like the number of clusters, multiplicity, total charge, position and time are extracted and used for the data analysis [27]. The number of clusters parameter is simply how many clusters are recognized within the time for one signal - every event should consist of one anode cluster and one cathode cluster. Multiplicity is the number of hits the cluster is made of. Total charge is calculated by adding the charge accumulated for each individual hit. Position is the center of the cluster, and time is the mean time of the cluster, calculated by getting the charge weighed mean of the positions and times of individual hits that make up the cluster respectively.

Every four hours, the TPC automatically takes calibration data with the ^{55}Fe source mounted inside the shielding. This source normally rests behind a lead shield, but during the calibration it is moved in front of each of the bores for five minutes to take the calibration data. Using this data and the known peaks of ^{55}Fe, the energy calibration of the observed signal is made.

6.2. CCD detector

The CCD detector [22] is a solid state pixel detector which has very high precision for position and energy measurements (Figure 6.5). There are 200 horizontal pixels and 64 vertical pixels in the rectangular region of 30.0 mm×9.6 mm occupied by the CCD. This amounts to each pixel having 150 μm×150 μm area.

[21] While having an anode cluster without a cathode cluster is unthinkable, for the analysis, this kind of classification is neccessary.

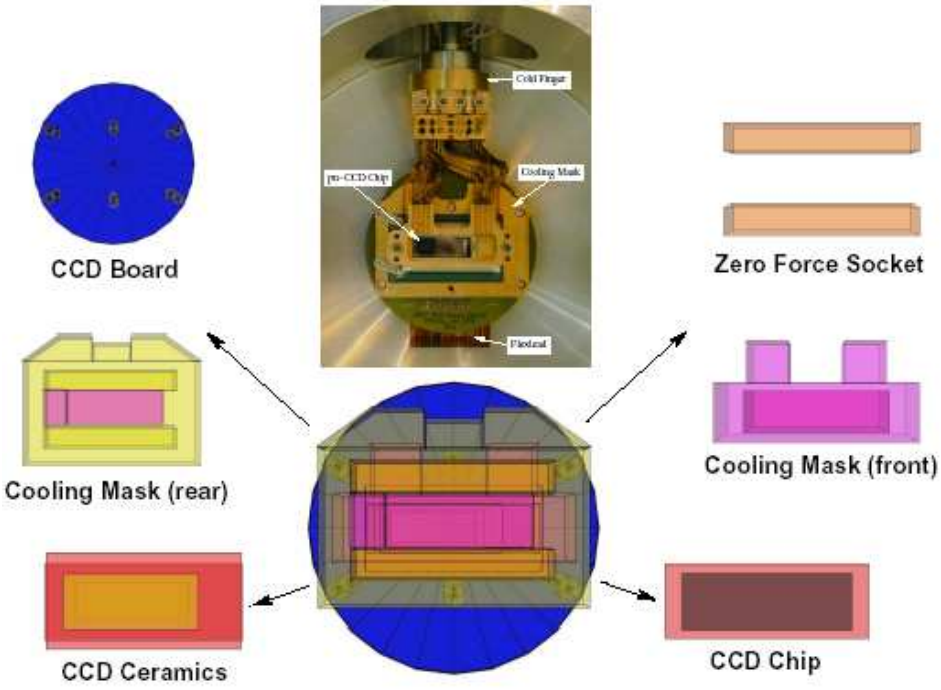

Figure 6.5. The CCD detector

Compared to other CCD's, the CCD in CAST has a very fast readout. This is because all of the 64 channels in the vertical are read simultaneusly. While the data read from the first 64 channels (or first 64 pixels) are being sent to the computer, the columns are shifted once so that the readout channels are occupied now with the next 64 pixels. This procedure is repeated 200 times within 6 ms, so that all of the 200 rows are read and fed to the computer. The feeding process repeats itself every 71 ms, which allows time for accumulation of charge on the specific pixels. Of course if a hit occurs during the shifting period of the pixel data, it will be seen in the wrong place, but the error is still low enough, since the shift time is much less than the waiting time, but still, a correction is made for this in the analysis program.

Unlike the gas detectors, the definition of noise in the CCD is a bit different. There exists a dark current for each of the pixels, equivalent of the pedestal in the other detectors; and the standard deviation of this dark current can be regarded as noise. The dark current - offset (O_{ij}) and the noise (N_{ij}) are both used in the analysis procedure with $0 \leq i \leq 199$ and $0 \leq j \leq 63$, defining each pixel's offset and noise.

Because of the reading procedure,[22] some of these data might not be perfect. These events which were recorded during the CCD readout are called the Out of Time (OOT) events. The time intervals that can be taken into account for the data analysis are called Good Time Intervals (GTI).

The background reduction is partly due to a Pb shielding and partly due to the x-ray telescope. After the inner Pb shielding was installed in 2004, the background was observed to be reduced by a factor of 1.5, from 11.5×10^{-5} photons/cm^2/sec/keV to 7.69×10^{-5} photons/cm^2/sec/keV, as expected (Figure 6.6) [21].

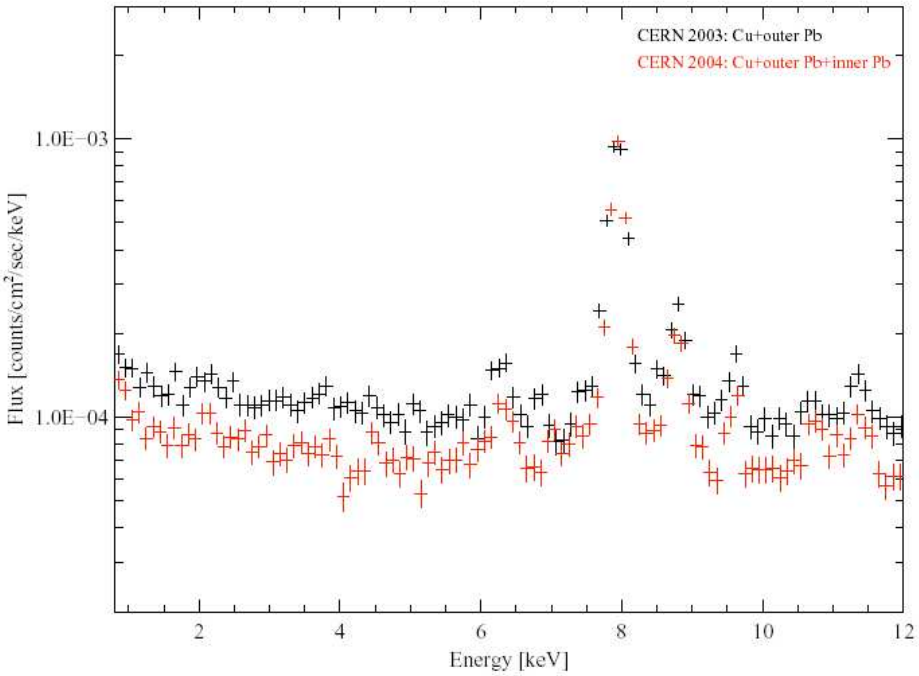

Figure 6.6. The improvement of the background in 2004 due to the Pb inner shielding. The data after inner shielding was installed are plotted in red

6.2.1. The X-ray Telescope

The photons coming from the bore which has a diameter of 4.3 cm are focused on the CCD by an x-ray telescope installed in 2003, actually a prototype for ARBIXAS space telescope. The telescope is composed of 27 concentric mirror shells (Figure 6.7) which reflect the EM radiation twice, the first time being from the parabolic, then the

[22]The shifting of the pixel charges in order to be read by the FADC's.

hyperbolic mirror, resulting in a focal length of 1.7 m. As a result, the beam is focused on the CCD, allowing much better background reduction and precision. Of course, the transmission rate of the telescope[23] results in the detection to be somewhat less efficient due to the decreased signal. On the other hand, having practically no background in the CCD-Telescope system dramatically increses the chance to correctly identify a signal.

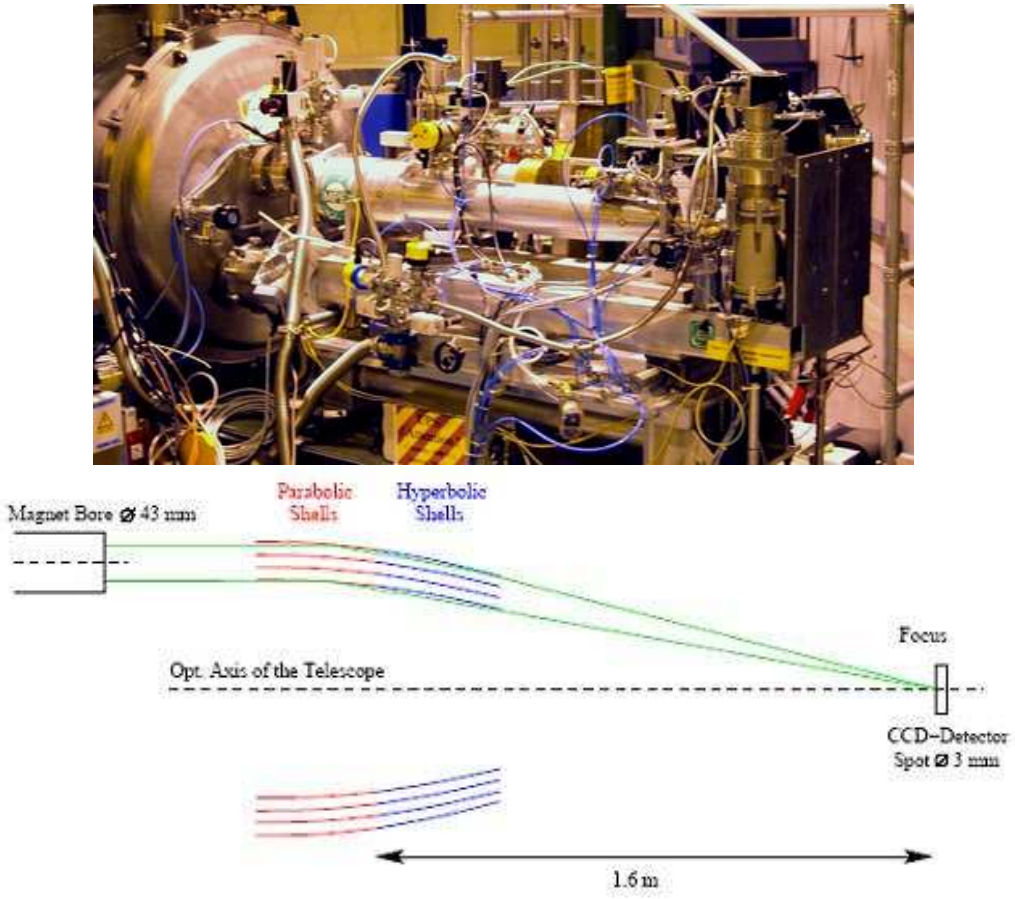

Figure 6.7. The x-ray telescope for the CCD

The CCD-Telescope system has very delicate operating conditions. Both the pressure and the temperature has prescribed maximum values for smooth operation without damaging the components. The temperature is set at 120 K, while the pressure system is regulated by a dedicated computer which gives off alarm and shuts down the

[23]Transmission rate of the telescope is 35%

interior valves if the vacuum requirements of the telescope or the CCD are not met[24] , or if one of the vacuum pumps stops working. There are three vacuum pumps dedicated to the CCD and the telescope, and there is a complicated valve/pump network (Figure 6.8), (Figure 6.9).

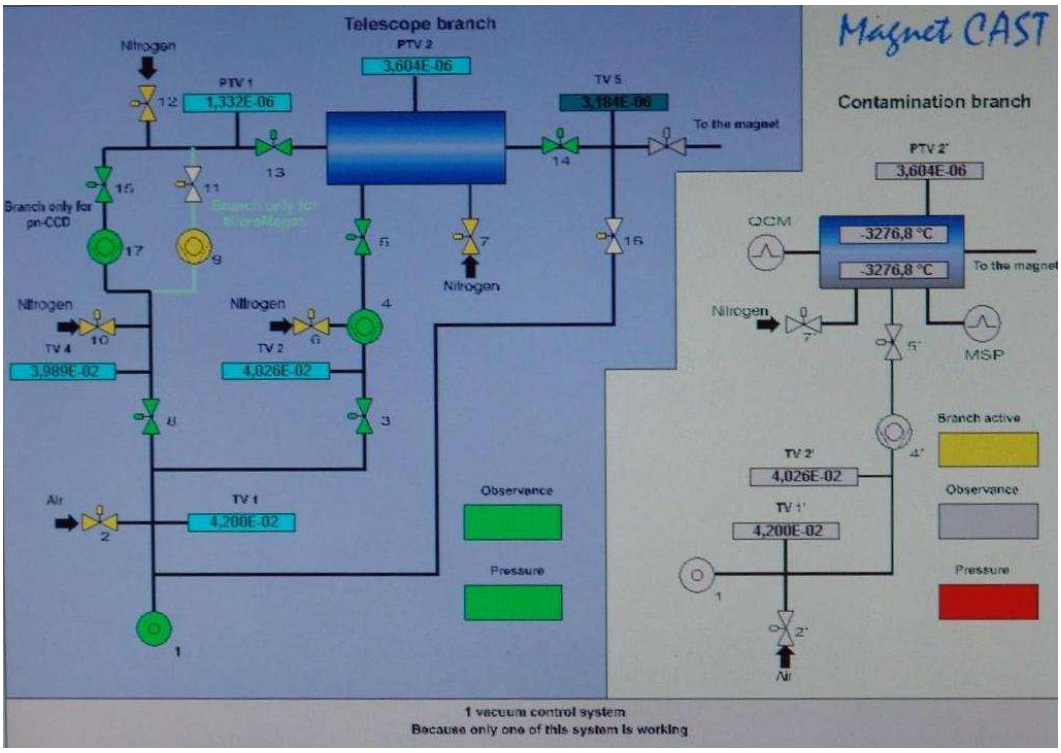

Figure 6.8. The valve/pump network program of CCD and the telescope

Since the telescope is not specifically made for CAST, the radius does not exactly fit the bore of the magnet. Actually, only one of the six sectors of the telescope was more than enough for covering the bore. Thus, using only one sector, the focusing of the beam onto the CCD was accomplished. The obvious question of why the middle of the telescope was not used instead of one of the sides also has an obvious answer, since the mirror arrangement can only provide focusing for the sides and not for the middle.

On the other end of the bore that the telescope is mounted on (on the TPC side) an x-ray finger source was installed to make calibrations. This x-ray finger source is retractable and during the tracking it is totally hidden in order not to affect the

[24]The pressure requirement for smooth working is at most 10^{-6} mbar for the system.

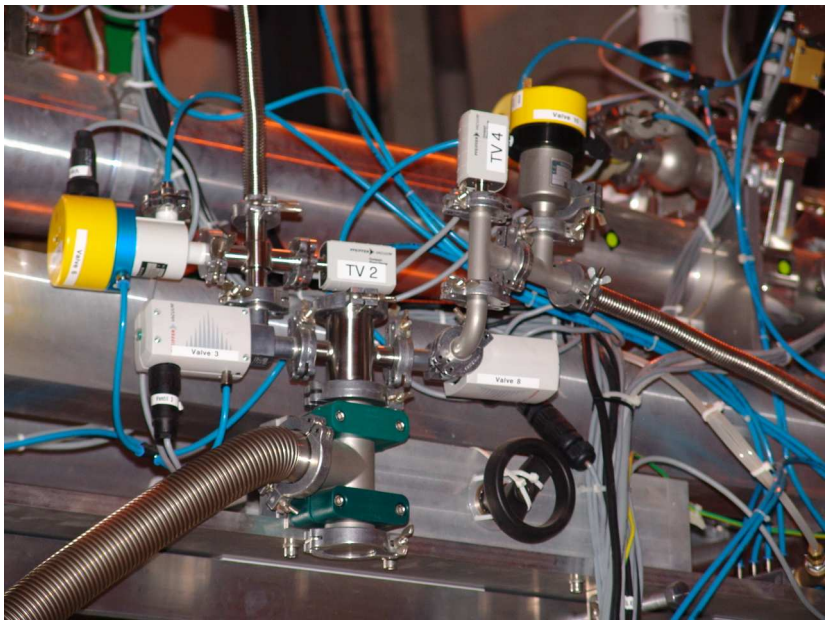

Figure 6.9. A photograph of the valve network of the pressure system of CCD-Telescope. Note the pressure sensors are labeled as TV# just as they are labeled as PTV# in the program

data. Since it retracts to the side, the finger can be positioned almost anywhere in the horizontal plane within the bore, while in the vertical no movement is possible.

6.2.2. Alignment of the X-Ray Telescope

The x-ray telescope in front of the CCD detector had to be aligned for Phase II, the data taking in 2005. For this, all of the changes that were made for the second phase had to be taken into account [25]. One such change was that the cross-hairs that were inside the cold bore in Phase I were removed in order to install the cold windows. This resulted in a need for a new reference optical axis. Another difference is that the laser beam used for the alignment procedure was shifted by 0.5 mm in order to align it with the new optical axis. Of course, during the alignment for the Phase II, there was ^{4}He in the cold bore also.

The procedure for the alignment was mostly the same as the 2004 alignment. After the magnet was moved to the H = 20158 and V = 26493 position, and the

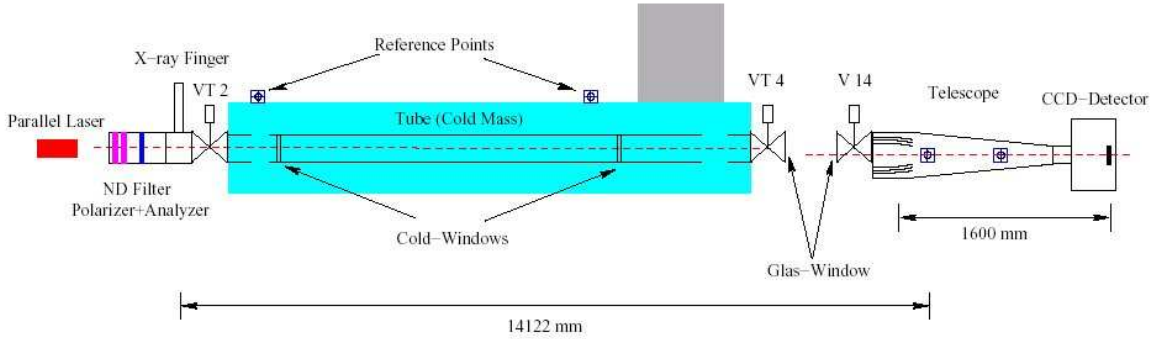

Figure 6.10. The alignment setup of 2005

orientation is furter checked by using the reference points placed on the magnet (Figure 6.10). The axis defined by the center of the circular openings of the bore on each end is found to be horizontal with a 0.2 mm precision. This axis was the optical axis in Phase I. All measurements were made with respect to this line both in Phase I and Phase II. The next step was making sure the telescope was not moved during the time between the last alignment and this one. The three stickers on the telescope provided a means to check this. A new optical axis was defined as passing through the center of the strongback pattern on the cold windows, after measuring the position of this center point for all windows both horizontally and vertically.

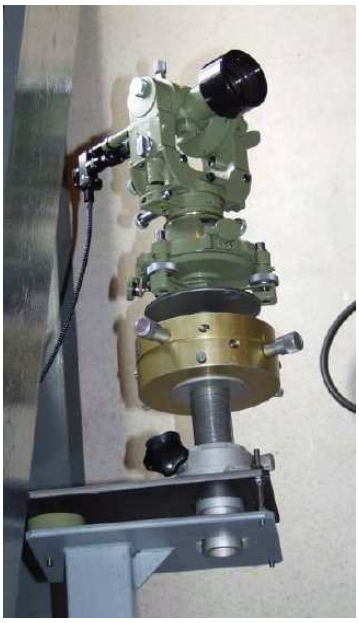

Figure 6.11. Photograph of the theodolite employed for the alignment

A thedolite[25] (Figure 6.11) was used to measure the target that was placed on the telescope flange, both through the bore and from an external region, so that the effect of cold windows and the ^{4}He gas can be observed, if any. After it was made sure that the optical axis defined by the center of the two cold windows was aligned with the theodolite (with an accuracy of $\pm$ 0.2 mm) by visual examination through the theodolite, the laser was connected to the theodolite via fiber-optics, thus the laser light was focused on the target on the telescope flange. It was made sure that the laser spot rested in the middle of the crosshair.

The collimation of the laser beam was made by installing a corner cube prism (Figure 6.12) between the cold bore and the telescope, which allowed checking the parallelism of the beam both in itself and to the optical axis, since the corner cubes always reflect back parallel to the incoming beam.

[25]A theodolite is a device which produces a wide parallel beam from a laser light or focuses it at one point, measures angles and displacements precisely.

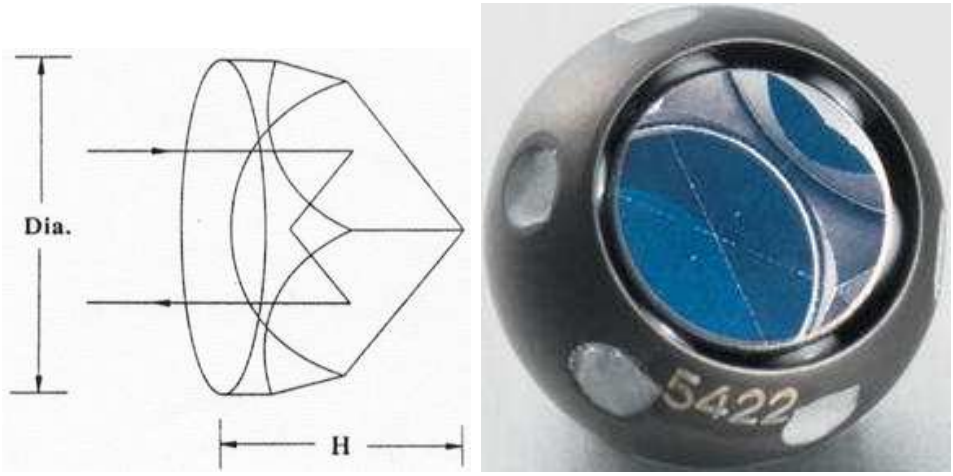

Figure 6.12. A corner cube prism similar to the one used for collimation

The beam is dimmed with polarizing filters and the spot is observed on the CCD. The location of the spot was determined. The location of the spot for the x-ray finger source was also determined on the CCD and the results were compared both to each other and with the alignment data of 2004 (Figure 6.13).

Upon comparing the data, it was seen that the laser spot in this alignment procedure was seen, on the average 7.57 pixels away from the spot of the last alignment procedure in 2004. This was quite a mystery, since the x-ray spot[26] did not present any change in position. (Figures 6.14, 6.15, 6.16) This obviously led to some tests to check the alignment procedure, the theodolite, the windows and the telescope. Several theories were suggested:

6.2.2.1. Abberations of the Telescope. The telescope - although not refractive in nature - may have produced some abberations which would result in such a behaviour when the beamline is parallel shifted. On the other hand, this result should not differ for x-rays, since the telescope only uses reflection for focusing, which will not behave differently for x-rays.

[26]The x-ray spot was produced by the x-ray finger source mounted at the TPC side of the cold bore.

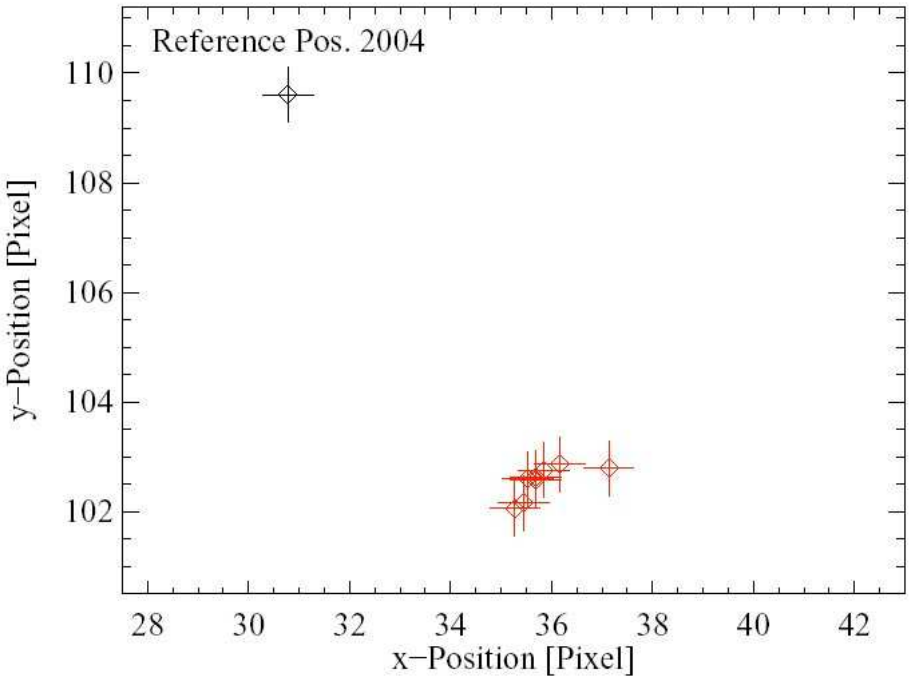

Figure 6.13. The spot positions for different intensities of the laser beam

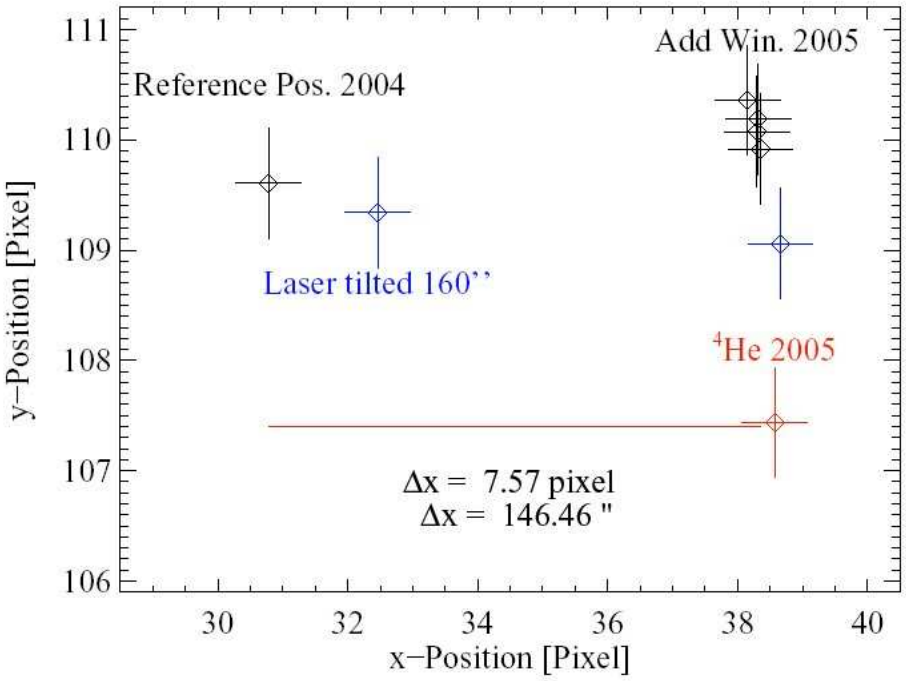

Figure 6.14. The results of the alignment procedure before and after the insertion of the cold windows, and addition ^{4}He at 2 mbar of

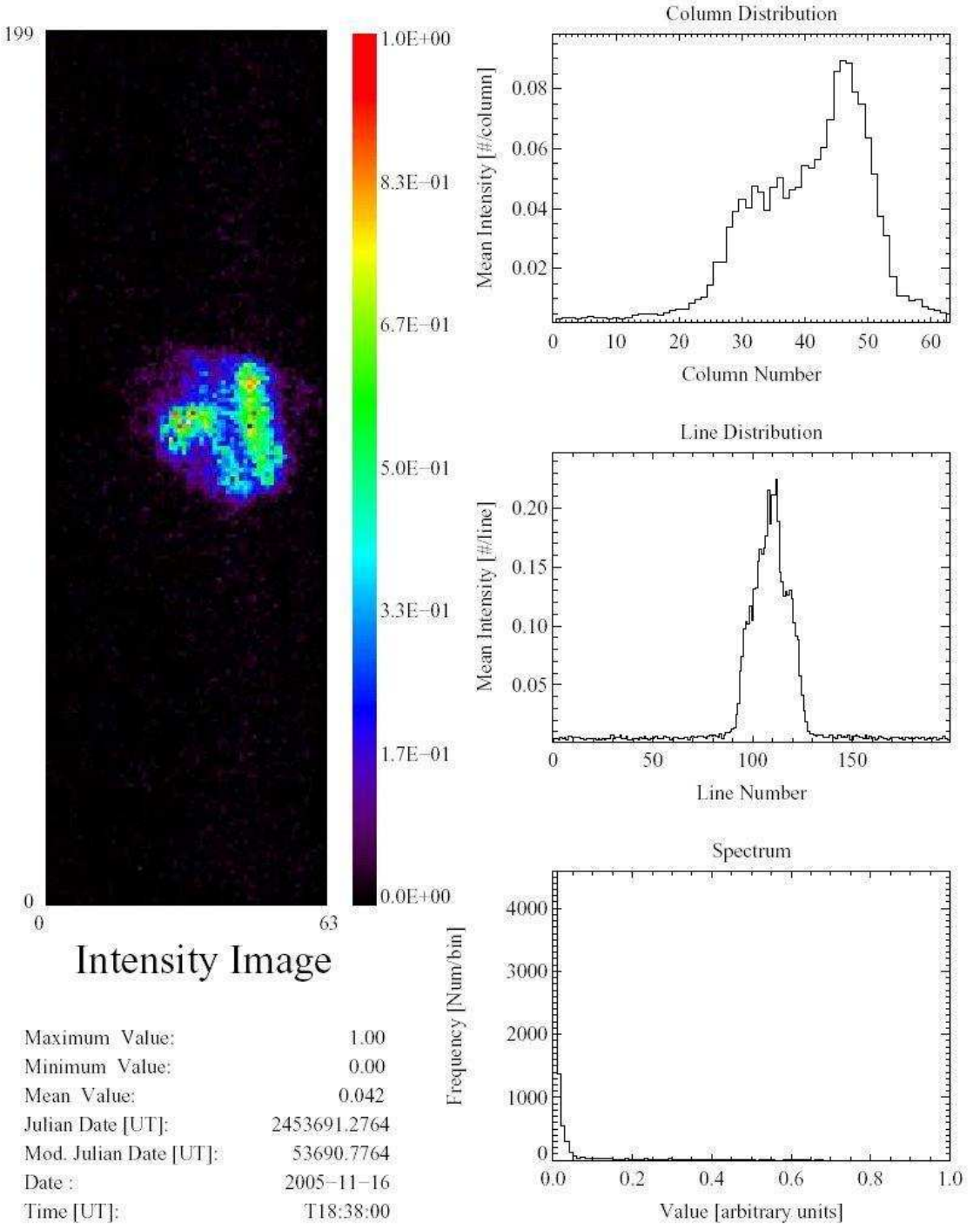

Figure 6.15. The laser spot as was in 2004 and the x-ray spot superimposed

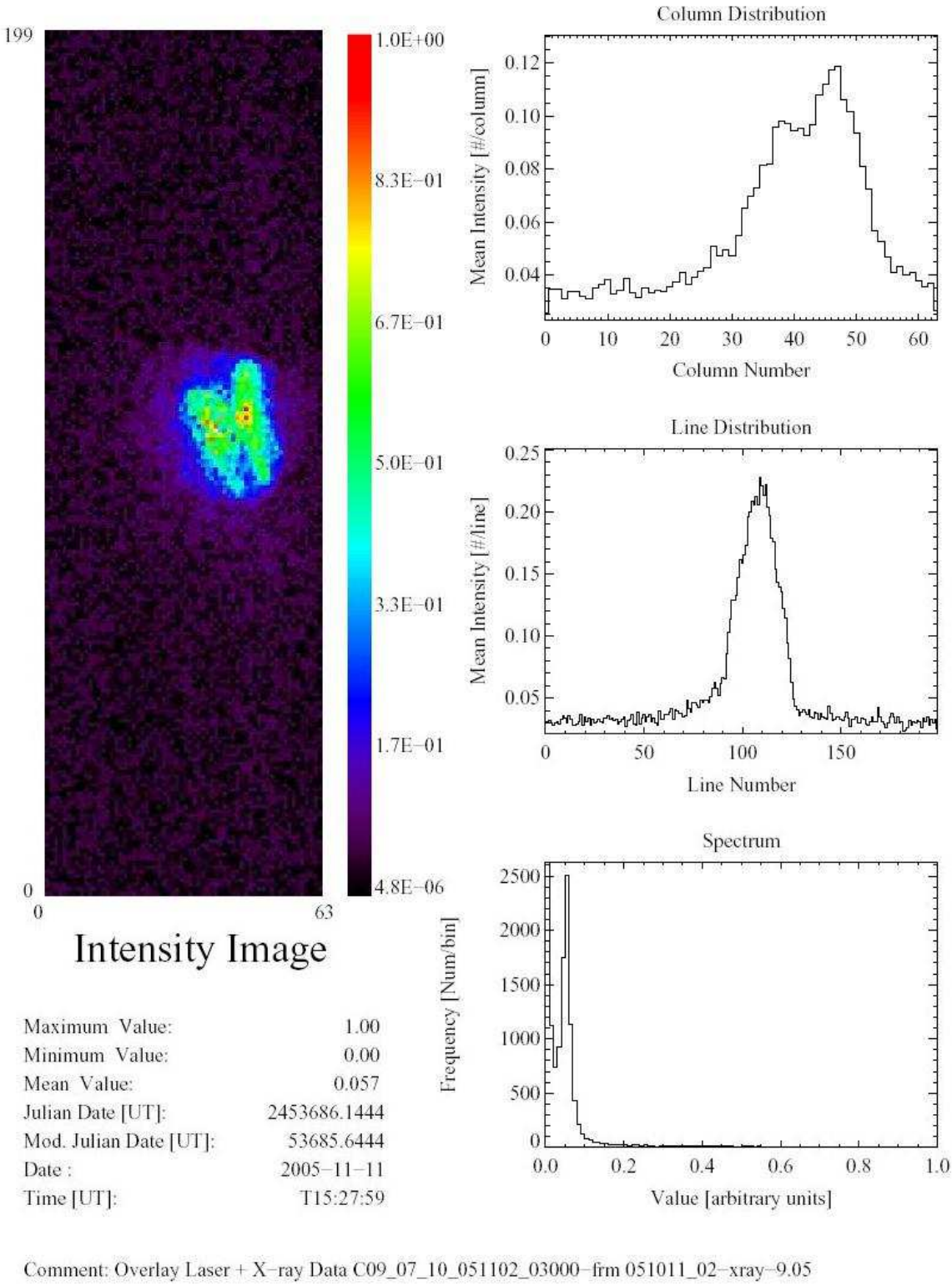

Figure 6.16. The laser spot in the last alignment (2005) and the x-ray spot superimposed

6.2.2.2. Refraction on the Cold Windows. The cold windows have a thin film of polyproplene which is bent by the pressure difference. This bending effect might have produced a shift in the position of the spot. However, for mainly two reasons this theory can also be discarded. First of all, the beam is far too wide for the small bumps in the cold window foil to cause a shifting effect; and secondly, even if the beamline was narrow enough, the actual effect does not change for further parallel shifts of the beam whereas it should have.

This has been checked by covering parts of the beam, namely the upper half, lower half, upper quarter, upper 3/4, lower 3/4, lower quarter, and left parts. The results can be seen in Figure 6.17.

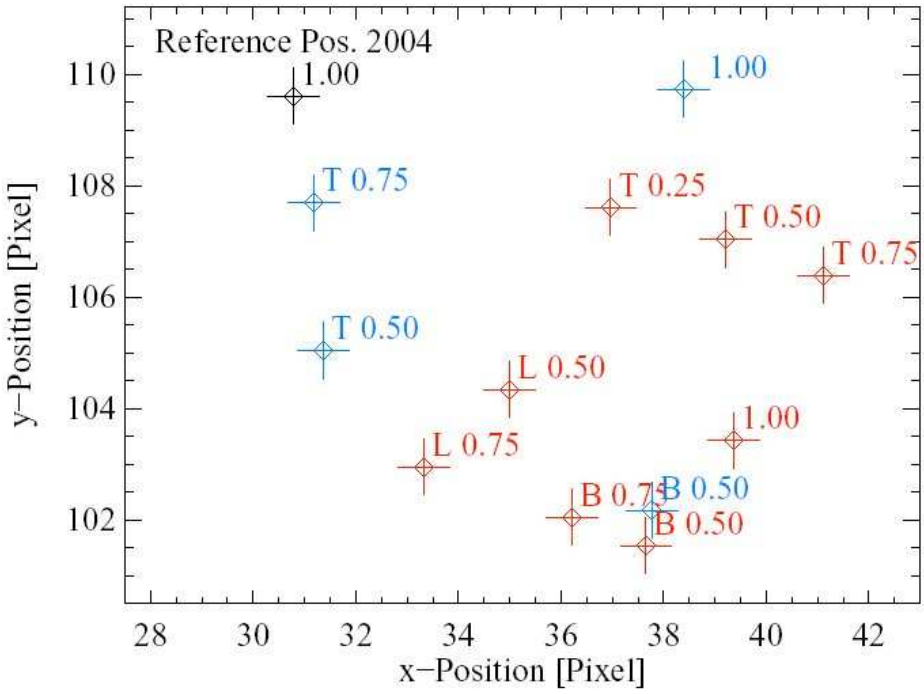

Figure 6.17. The observed laser spot position while parts of the beam (i.e the cold bore) were covered. Uncovered parts are indicated by, 'T' for top, 'B' for bottom, 'L' for left. The numbers indicate the percentage of open space, e.g. 0.75 means 75% open

6.2.2.3. The Conlcusion for the Spot Shift. The reason for the laser spot to be in a different position while the placement of the x-ray spot is unchanged leads one to

think of refraction, where the x-rays and the visible light behave differently. Since the telescope does not make use of any refractive lenses, this can only be explained by the refractive properties of the windows and/or the gas inside. It is obvious that any effect directly connected to the windows is negligable, however even a simple 0.1^o misalignment when mounting the windows will produce a prism of the gas that is trapped inside, causing the visible light and the x-rays to refract differently. Even if the windows are placed perfectly perpendicular to the cold bore, a simple temperature gradient within the cold bore can change the refractive index of the gas to produce an effect such as that was observed.

However, the important point to note is that the x-ray spot is not displaced with respect to the alignment in 2004. Since the experiment is aimed to detect photons in the x-ray region, whatever the reason it is that causes the visible light to bend, if it does not affect x-rays, it does not produce a problem for the well being of the experiment, and since it was confirmed that the x-ray spot has no displacement whatsoever, we can ignore this problem.

6.3. MicroMEGAS Detector

The first MicroMEGAS detector was developed by Giomataris and Charpak in the 90's for applications in particle physics. With the latest development efforts however, the initial design is much improved, resulting in a detector that has a spatial resolution less than 100 μm, energy resolution better than 14% for the energy range of 1-10 keV, in which the CAST experiment searches for the axion [30, 31].

Basically, the MicroMEGAS detector is a gas chamber, and the spatial resolution is better than the TPC. As can be seen from Figure 6.18, the photons coming from the cold bore first enters a buffer region of He (in the case of CAST, vacuum) before going through the window into the active volume of the detector. The active volume is defined by the region where the ionization takes place, and it is filled with Ar-isobutane

mixture with the isobutane ratio being 5%. The ionized electrons drift towards the micromesh, because of the applied 1 kV/cm electric field. On the other hand, after passing through the mesh, the electric field increases dramatically, up to 40 kV/cm and the electrons create an avalanche towards the strips.[27]

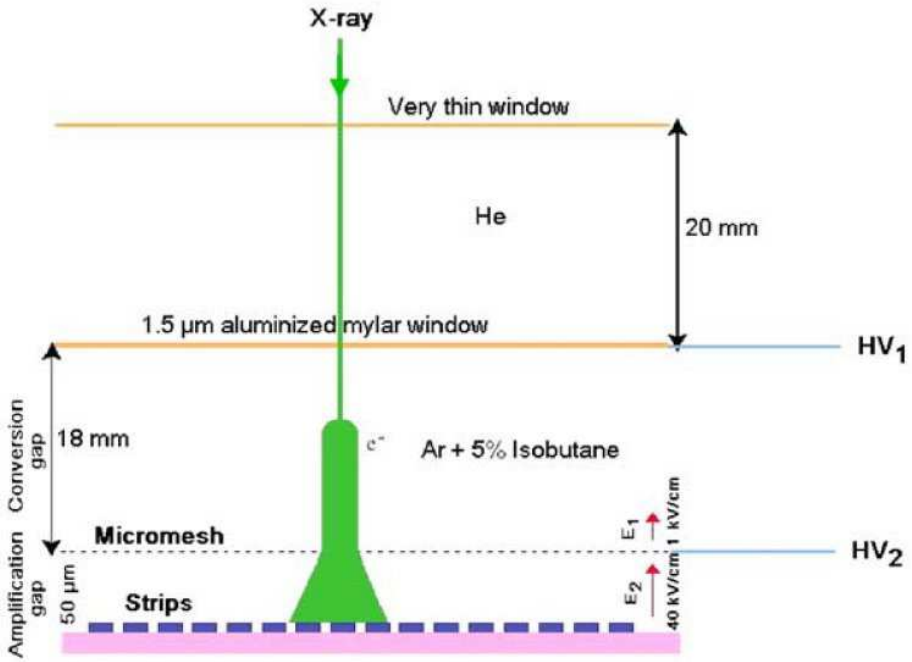

Figure 6.18. The working principle of the MicroMEGAS detector

The micromesh has 25 μm holes that are 50 μm apart, allowing the secondary electrons to pass through. This signal from the micromesh is read out by Flash Analog to Digital Converters (FADC). While the active region before the mesh has a thickness of 18 mm, the avalanche region between the mesh and the strips is only 50 μm thick. This thickness is maintained uniformly over the readout strips to ensure stability and uniform gain which is 10^4 (Figure 6.19).

As can be seen in Figure 6.20, the MicroMEGAS detector reads the 192 X and 192 Y strips via four readout cards, each of the cards is connected to half of one of the sides of the detection area, which is shaped like a rhombus. The position resolution of the strips is about 70 μm, since a signal can only be observed as a cluster and

[27]The distances that these electric fields are applied to are 18 mm and 50 μm for the 1 kV/cm and 40 kV/cm respectively. The fiels result from the voltages applied to the strips and to the window, which are 200 V and -1800 V respectively, and the mesh, which is grounded.

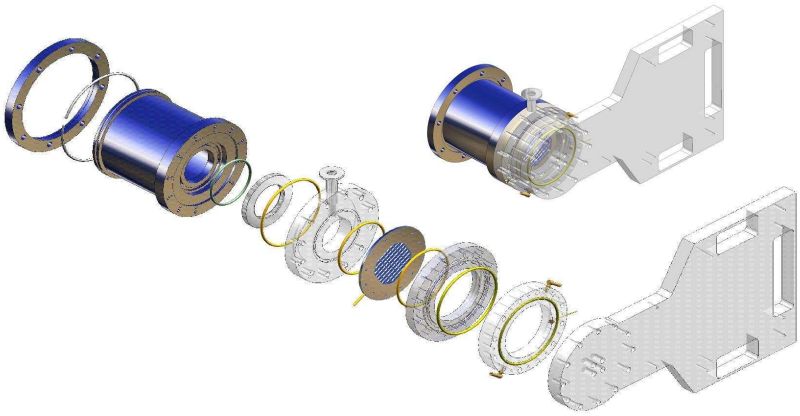

Figure 6.19. A schematic diagram of MicroMEGAS

calculation of the barycenter of this cluster can give a better value than even the strip seperation, which is about 350 μm.

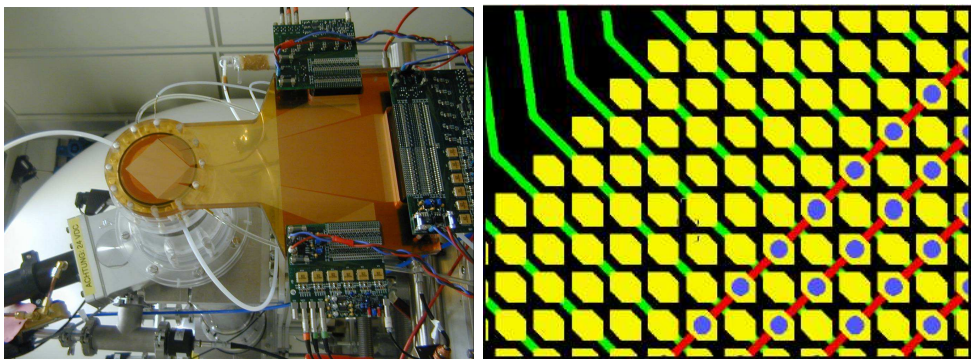

Figure 6.20. *Right*: The MicroMEGAS detector before it was installed on the cold bore. *Left*: The strips of MicroMEGAS up close

The parameters that are extracted from the data for the events – although similar to the other detectors, are defined differently. The clusters are defined as the strips that give signal which have less than three strips between them, for example. Multiplicity is similar to the previous definition, however a minimum multiplicity is defined also, which is three. The charge is the total charge of the cluster, and centroid is the central strip of the cluster.

The triggering of the detector is made by a signal obtained through the use of a preamplifier connected to the mesh. While the NIM modules regulate the data acquisition, high voltage and trigger, the actual data taking is done by the VME

modules. The NIM and the VME crates are located beside the CAST magnet, as close to MicroMEGAS detector as possible (Figure 6.22 Left).

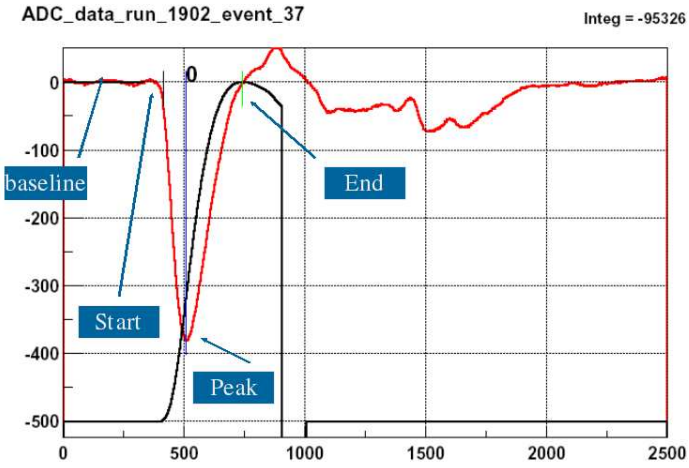

Figure 6.21. Some of the parameters used for selecting or rejecting a pulse in the FADC system of MicroMEGAS

The pulse coming from the detector first has to be selected by the FADC units in order to be sent to the analysis programs [32]. A number of parameters are extracted like: start, peak, end, rise times; pulse, rise, default integrals; amlitude; the ADC units for the baseline and the fluctuation; and pile up. Some of these parameters are used for rejecting a pulse, looking at the treshold crossing point, comparing the baseline and the fluctuations with the previous samples, the absolute minimum of the peak, the start of the pulse, the risetime - which must be 10% to 90% of the pulse for it to be selected - the end of the pulse, the pile ups and the cumulative distributions - the pile ups (Figure 6.21).

Of course, some of the electronics are obviously located near the detector, and are quite sensitive. It was required that this immediate electronics to be shielded from the electromagnetic interference. For this reason, a Faraday cage was installed, covering the essential equipment, not allowing the interference to affect the system (Figure 6.22 Right).

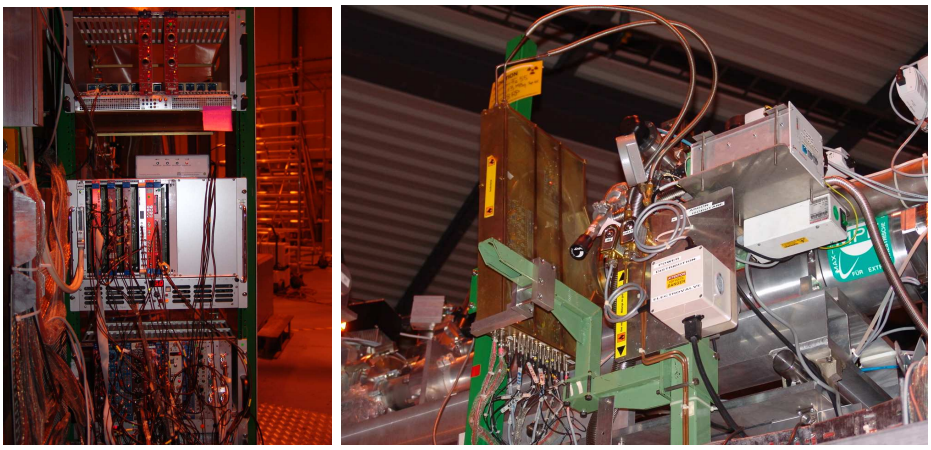

Figure 6.22. *Left:* The NIM and VME modules of the MicroMEGAS detector. *Right:* The Faraday Cage covering the immedeate electronics of the MicroMEGAS system and the gas system

The data taking takes place for 23 hours per day. The remaining time is spend for pedestal and calibration runs. For the pedestal run, the trigger is made by a random counter and the high voltage is off. For the calibration run, the only difference from the normal data taking is that ^{55}Fe source is positioned behind the detector. In Figure 6.23, the ^{55}Fe source and the detection area of the MicroMEGAS can be seen with the four holes arranged as a square. These holes help monitoring the spatial resolution. These calibration and pedestal runs are taken just after the morning tracking (during sunrise), where the supposed axion signal would be seen.

The conversion efficiency of the MicroMEGAS detector was 73% in 2003, however with the changes in 2004, the efficiency rose up to 88%. These changes most fundamentally involved installing an upgraded version of the detector with a new strip structure causing less cross-talk, casing containing less Cu therefore causing less x-ray emission, a new VME digitalizing board and an automated calibration source.

The pulse coming from the detector first has to be selected by the FADC units in order to be sent to the analysis programs [32]. A number of parameters are extracted like: start, peak, end, rise times; pulse, rise, default integrals; amlitude; the ADC units for the baseline and the fluctuation; and pile up. Some of these parameters are used

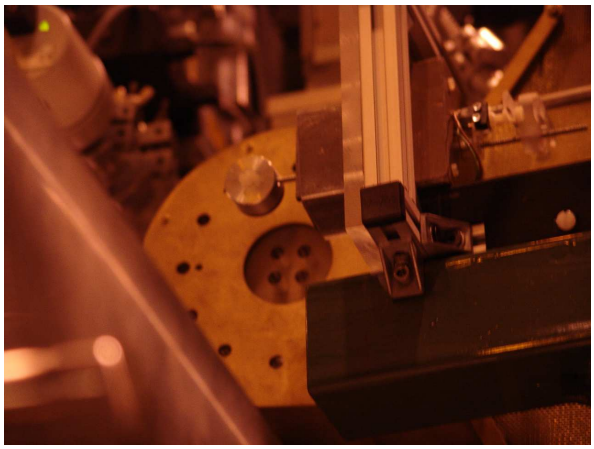

Figure 6.23. The ^{55}Fe source used for the calibration of the MicroMEGAS after each tracking run every day

for rejecting a pulse, looking at the treshold crossing point, comparing the baseline and the fluctuations with the previous samples, the absolute minimum of the peak, the start of the pulse, the risetime - which must be 10% to 90% of the pulse for it to be selected - the end of the pulse, the pile ups and the cumulative distributions - the pile ups (Figure 6.21).

7. ANALYSIS

There are two analysis procedures for each detector. One kind of analysis is called the online analysis, and takes place during the data taking, which allows the shift people to check that the detectors are working correctly. The other kind of analysis is called the offline analysis, and obviously that is where the data are analysed to search for the axion signal. The online analysis programs both for the TPC and for the MicroMEGAS can be used in parralel to the data taking, while the online analysis program for the CCD can only be used to check the detector before the data taking starts.

The offline analysis of each detector is done by using a fitting function proportional to $g_{a\gamma}^4$ [24], [26]. The fitting function used is the theoretical photon flux, multiplied by the detector efficiency as a function of energy, different for each detector. The fitting is done by using the standard χ^2 minimization for the MicroMEGAS and the TPC. On the other hand, for the CCD, a likelyhood fuction is used for the data taken within the spot where the axion signal is expected, because of the low statistics. The graphs of the specific fits and the 95% CL upper limits on these fits can be found in the relevant sections about the detectors:

7.1. TPC

Before going into any kind of analysis, some cuts have to be applied to the data in order to seperate the events from the noise. Table 7.1 shows these cuts and under which conditions are these cuts applied for the TPC detector [27].

Table 7.1. The cuts and the corresponding conditions that the cuts are applied for the TPC

Cut	**Condition**
single cluster	number of anode clusters = number of cathode clusters = 1
anode multiplicity	$1 \leq$ number of anode hits ≤ 3
cathode multiplicity	$2 \leq$ number of cathode hits ≤ 8
anode-cathode time difference	-0.15 μs $\leq$ time btw. anode and cathode clusters $\leq$ 0.02 μs
no saturation	no hit in the upper part of FADC range
anode/cathode charge ratio	around 1.85, energy dependent
coordinate cut	the position of the event should be within the range facing the bore of the magnet

After the cuts are applied and the irrelevant data are disposed, several variables need to be calculated for the analysis procedure for the TPC. The first of these variables is the expected axion flux on Earth:

$$\frac{d\phi}{dE} = 4.02 \times 10^{30} g_{a\gamma}^2 f(E), \tag{7.1}$$

where,

$$f(E) = E^3 (e^{-(\frac{E}{1.103}-1)}). \tag{7.2}$$

The conversion probability from Equation (2.21) and the efficiency of the detector (Figure 7.1) must also be multiplied with this value to calculate of the expected number of events.

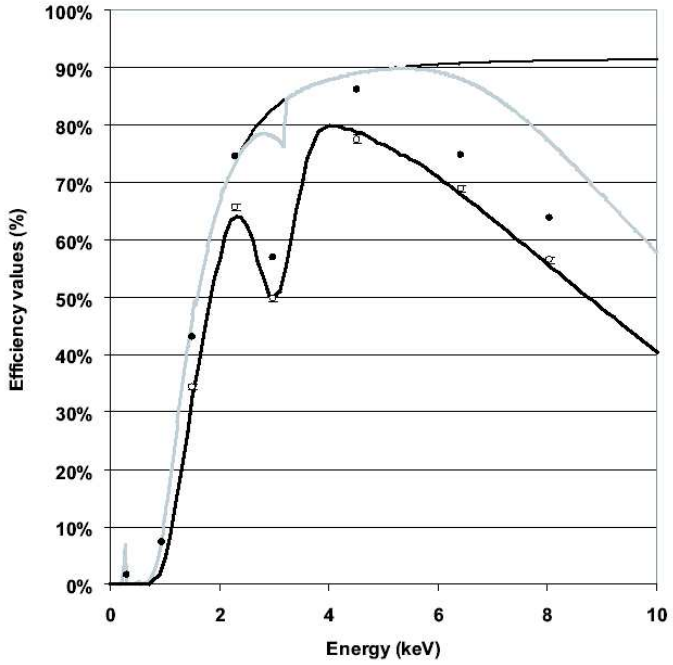

Figure 7.1. The efficiency curve of the TPC detector. The dots correspond to the experimental measurements of the efficiency of the TPC, before (black) and after (white) the offline analysis cuts are applied to the data. The upper thin black line represents the theoretical computation of the window transmission, while the grey line includes also the opacity of the gas in the chamber. The thick black line is an analytical function used to interpolate the experimental points in the final analysis

Lastly, one must add the dead time (2.5%) to the analysis. Thus, the χ^2 analysis will be as follows:

$$\chi^2 = \sum \frac{(x_{th} - x_{exp})^2}{\sigma_{exp}^2}, \tag{7.3}$$

where x_{th} is the spectrum calculated from the aforementioned axion flux, the conversion probablility and the efficiency, x_{exp} is the subtracted data[28] from the detector, and σ_{exp} is the poissonian standard deviation of the subtracted data, i.e. $\sqrt{x_{exp}}$. The theoretical value is proportional to $g_{a\gamma}^4$, since it is calculated by multiplying the incoming flux, and

[28]The background subtracted from the tracking data.

the conversion probability, each having a factor of $g_{a\gamma}^2$ in them.

This χ^2 value can be minimized by taking its derivative with respect to $g_{a\gamma}^4$ and setting it to zero. Thus, the value of $g_{a\gamma}^4$ for the minimum χ^2, and of course the χ^2 itself can be calculated.

To test the axion hypothesis, one must first test the null hypothesis to see if the data corresponds to the absence of the signal. For this, the theoretical values are taken to be zero, and the χ^2 is calculated by only using the experimental values.[29] The result is,

$$\frac{\chi^2}{dof} = \frac{27.4}{28}, \tag{7.4}$$

where the dof corresponds to degrees of freedom, or number of bins used in the classification of data. Looking at this value, we can say that the data is compatible with the absence of a signal.

When the best fit was calculated by using the proper χ^2, $g_{a\gamma}^4$ for the minimum χ^2 value is found to be negative, which is unphysical,

$$(g_{a\gamma})_{min}^4 = -(9.6 \times 10^{-11})^4 \,\mathrm{GeV}^{-4} \tag{7.5}$$

However, if we calculate the 95% CL upper limit on this value by looking at the integral,

$$0.95 = \int_0^{UL} e^{\chi^2/2} dg_{a\gamma}^4 \tag{7.6}$$

and pulling the required $g_{a\gamma}^4$ value, we find that,

$$(g_{a\gamma})_{up} = 1.46 \times 10^{-10} \,\mathrm{GeV}^{-1} \tag{7.7}$$

which is the 95% CL upper limit final result for the TPC.

[29] This is the same as setting $g_{a\gamma}$ equal to zero, i.e. no coupling at all.

7.1.1. Online Analysis

The dedicated computer for the TPC analyzes and plots the signal information simultaneously. The shift person can observe the calibrations and the signal online from the computer. The x-y coordinates of the observed events in the detector, the signal amplitude with respect to the position for the cathode and the anode wires, the counts per energy channel can be observed from the GUI (Figure 7.2). In case of the need for manual calibration arises, the shift person can use the same program to make a manual calibration, or if the automatic calibration starts during the tracking, again the shift person can take necessary steps to shut down the calibration procedure.

7.1.2. Offline Analysis

The offline analysis of the TPC detector was completed for the data set of 2003, and the results are published [24]. The analysis was limited to the mass range $m_a \leq 0.02$ eV because of the vacuum conditions.

In the analysis procedure, first of all the expected spectrum is calculated based on measurements and theory. Then, this function which is proportional to $g^4_{a\gamma}$ is used as the fitting function for the data set obtained by background subtraction from the tracking data.

With the installation of the heavy shielding of polyethylene, Cd, Pb and Cu, the background in 2004 dropped significantly. Reduced radon contamination due to flushing with nitrogen and the active muon veto system reduced the background even further and the data taking has become more efficient (Figure 7.3). The background was reduced by a factor if 2.4, from 9.27×10^{-5} to 3.85×10^{-5} photons/cm^2/sec/keV.

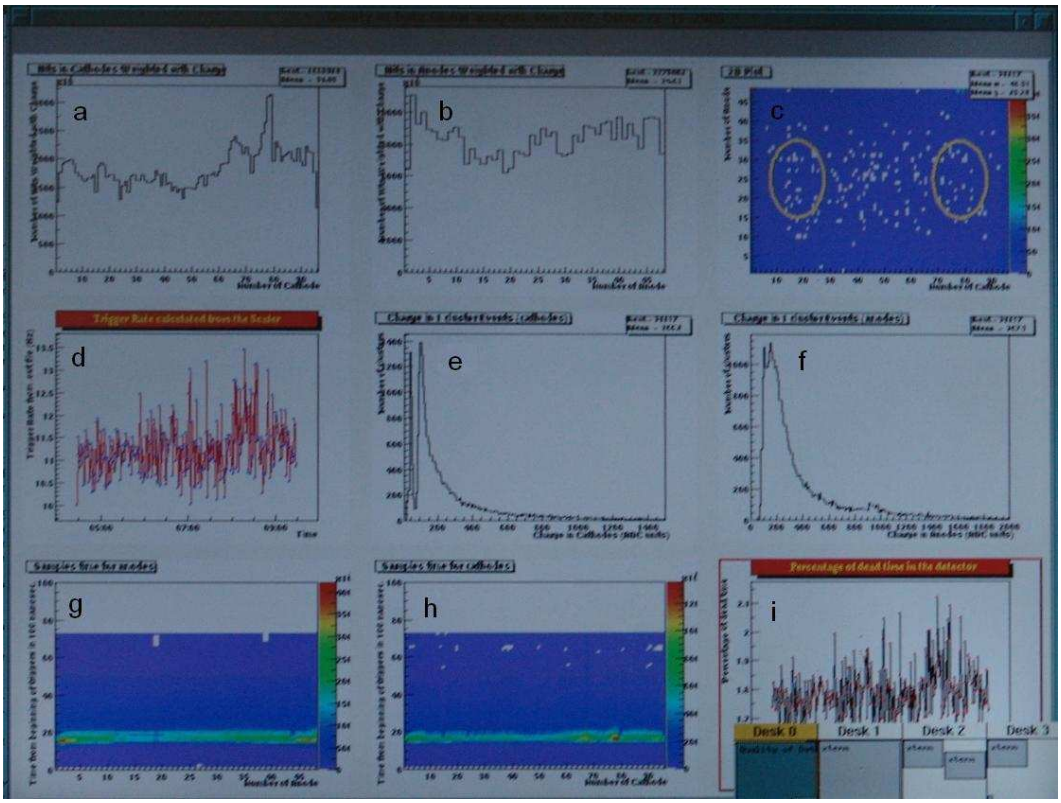

Figure 7.2. The main screen of the TPC online analysis program. Graphs are: a) Number of hits versus cathode wire number. b) Number of hits versus anode wire number. c) Anode wire number versus cathode wire number map with color scale defining number of hits. The yellow circles indicate the two bores from which the axion signal is expected. d) Trigger rate versus time. e) Number of one cluster events versus charge deposited in cathodes. f) Number of one cluster events versus charge deposited in anodes. g) Time beginning from trigger to 100 nsec versus anode wire number. h) Time beginning from trigger to 100 nsec versus cathode wire number. i) Percentage of dead time versus time.

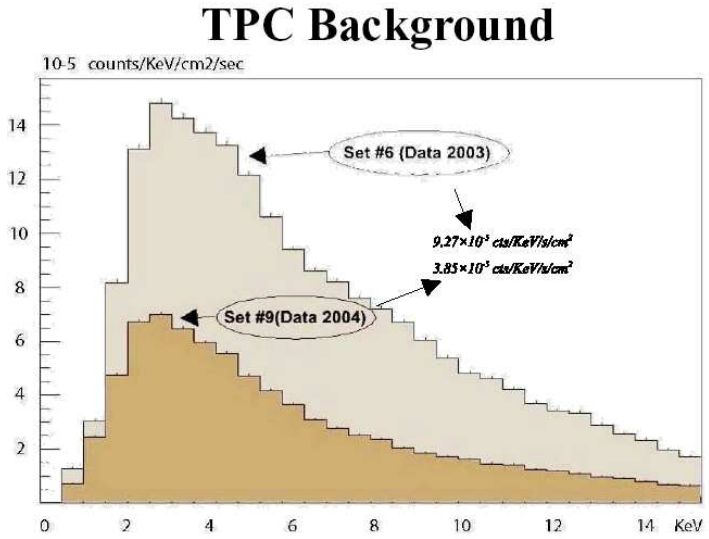

Figure 7.3. The improvement of background for the TPC in 2004

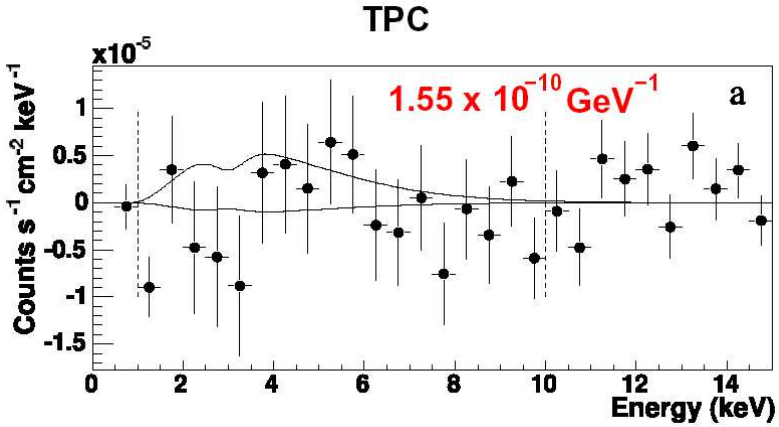

Figure 7.4. The results of the TPC 2003 data. The dots are the subtracted tracking data, the upper curve is the 95% CL limit on $g_{a\gamma}$ and the lower curve is the expectation for the best fit $g_{a\gamma}$

In the results, one sees a definite structure in the expected 95% CL upper limit on $g_{a\gamma}$ spectrum near the 2-4 keV region (Figure 7.4), however this is due to the change in efficiency due to the 2.9 keV Ar-K_α line in the spectrum. In other words, if the axion signal is too close to the Ar peak, it will be tricky to observe with the detectors that use Ar - basically both TPC and MicroMEGAS.

Apart from the expected structure in the 95% CL upper limit on the expectation value of the signal, no interesting phenomena can be observed in the data.

7.2. CCD

The calculation of the theoretical value for the expected data is almost the same as the TPC detector. The axion flux, the conversion probability, and the detector efficiency is multiplied to find the expected number of events for the CCD detector, too. On the other hand, the efficiency is defined a little differently.

There is no physical dead time for the CCD detector [28], instead, the data taken while the pixel charges are being shifted has to be regarded as "bad" data. Beacuse of the classification of the hits (which we shall see shortly) bands of one pixel width bordering the detector area also has to be excluded from the data.

Some cuts are applied to the data, for example, the data that do not contain any events above an energy threshold of 294.35 eV are discarded during taking of the data. While generating the spectrum, this threshold is further increased to 0.5 keV.

One difference of the CCD analysis from the other detectors is that it uses a pattern recognition algorithm. In general, the hits on the CCD can be classified in four groups: Single, double, triple, quadruple pixel hits. However the multiple hits can further be divided into other categories depending on the placement of the pixel hits with respect to each other. Of course, some of these combinations are impossible for a single hit of a photon, like having two pixels diagonally for a double hit. These combinations are discarded. The valid combinations can be found on Figure 7.5.

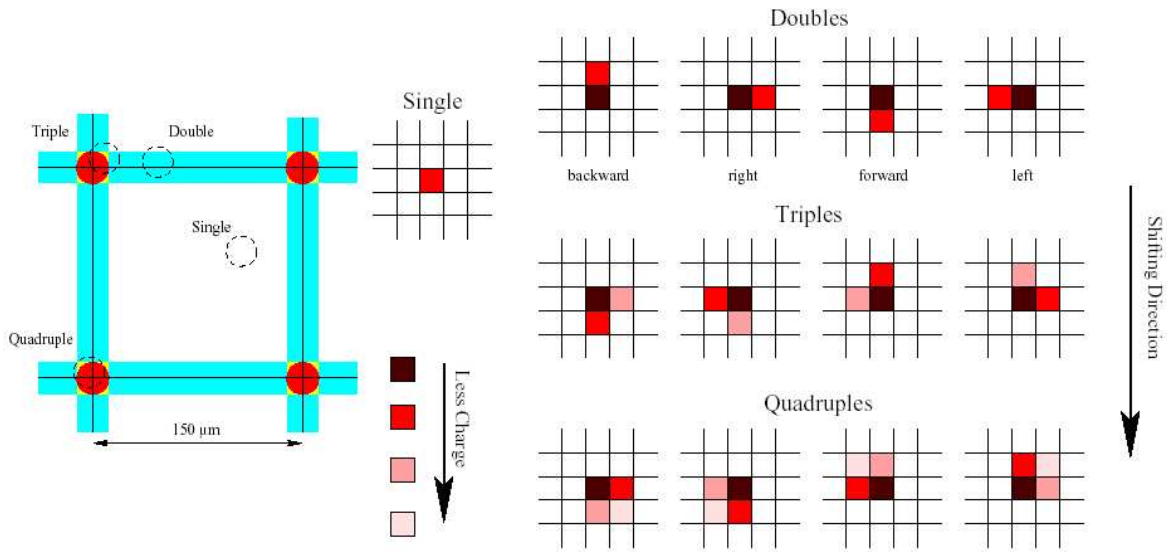

Figure 7.5. The valid geometries for the multiple hits on the CCD detector

While defining the GTI's slow control data has to be used. This allows us to define which data set belong to the tracking data (GTI's), and which belong to invalid data. The parameter used to define these GTI's are the magnetic field strength (MAGB), the supply voltage of the horizontal motor (HMOTV) and the flag for tracking (TRACK),[30] the times for the quenches (QUENCH), status of the gate valves (VTXOPEN), and the time stamp (TIME). Of course, when the magnetic field is down, there was a quench, or the gate valves are closed, no meaningful data can be taken. If the horizontal motor is not working, the tracking program is not active, or the time is during evening tracking, the data taken cannot be defined as tracking data.

Compared to the gas detectors, CCD has very low statistics, which result in the χ^2 analysis not being able to be used. Instead, a likelihood function is defined,

$$\mathcal{L} = \prod_{i}^{20} e^{-\mu_i} \frac{\mu_i^{n_i}}{n_i!} \Big/ \prod_{i}^{20} e^{-n_i} \frac{n_i^{n_i}}{n_i!}, \tag{7.8}$$

[30]Only the combination of HMOTV and TRACK can give a parameter that truly defines the tracking times.

where the i is the bin index, n_i is the experimental counts per bin and μ_i is the theoretical fit function. This likelihood function behaves quite similar to the χ^2, so it might be used similarly, to compare as confidence level. Since the μ_i also has the $g_{a\gamma}^4$ factor, it can be maximized just like the χ^2 is minimized, by taking a derivative and setting it equal to zero. The procedure is done by the MINUIT program to find a fit and the $(g_{a\gamma})_{min}$, and the 95% CL upper limit.

7.2.1. Offline Analysis

The offline analysis of CAST's CCD data for 2003 is complete. The results are posted on a web page [23] and are only accesible by the collaboration members, however the publication can be reached easily [24]. This publication not only shows the results of CCD data, but all the detectors. Since the results given in the publication are quite condensed, we will give more detail in the following pages.

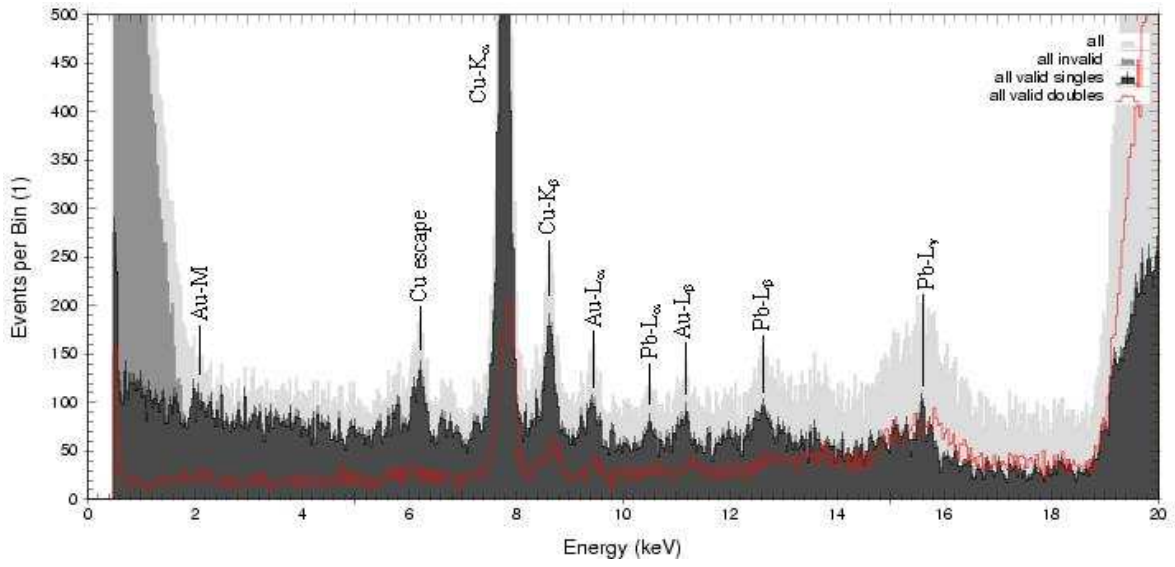

Figure 7.6. The background spectrum of CCD in Phase I, 2003 data

First of all, one must know the background spectrum of CCD to make any relevant analysis (Figure 7.6). The background is mainly the Cu-K$_\alpha$ x-rays at about 8 keV, but there are other prominent peaks also, like Cu-K$_\beta$ line and Cu escape peaks.

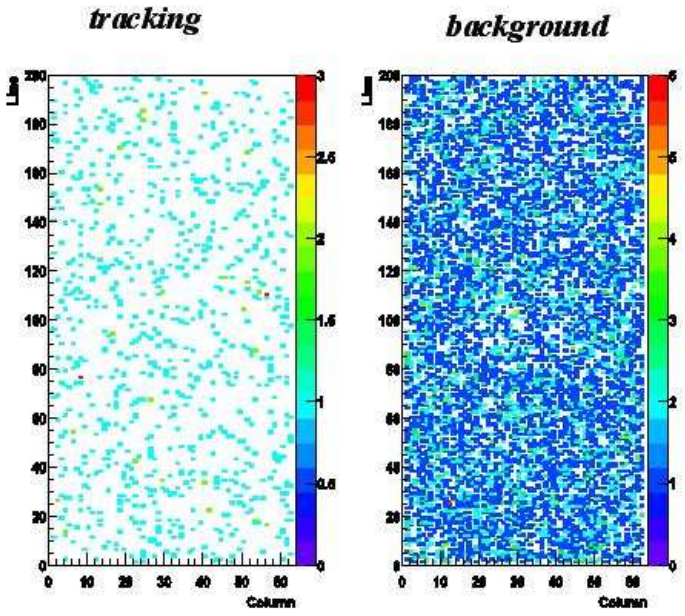

Figure 7.7. The difference between tracking and background in the data of 2003

As the data for 2003 was analysed, no significant difference was seen between the background and the tracking, for 77 hours of tracking and 810 hours of background data (Figure 7.7). As for the 2004 data, eventhough the analysis is not yet complete, the data consists of 196 hours of tracking and an effective 1500 hours of background, which should yield a significantly more accurate result than that of 2003 data. In Figure 7.8, one can see total counts in 54.3 mm^2 spot area in 121.3 hours of exposure, versus energy in keV [24].

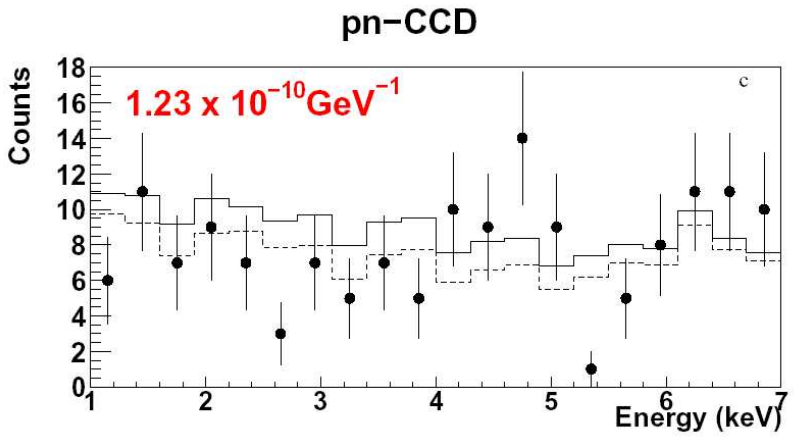

Figure 7.8. The analysis results of the 2003 data for the CCD detector. Dots are the the tracking data, dashed line is the background and the solid line is the expected tracking plus background with 95% CL for the $g_{a\gamma}$

In the 2003 data that was analysed, the stability of the telescope was not monitored, but in the 2004 data it was, with the alignment procedure. Therefore, a larger area was monitored for the tracking runs in 2003 than that in 2004. This is one of the possible reasons that the results of 2004 will be more accurate.

7.3. MicroMEGAS

The MicroMEGAS detector, being very similar in nature to the TPC detector, also show very close characteristics in the analysis procedures. The calculation of χ^2 and the minimization procedure is almost exactly the same, apart from the efficiency of the detectors of course [29].

One difference the MicroMEGAS detector has, is that during the 2003 data taking period, the detector itself has undergone some fundamental changes. This resulted in the data sets to be divided into three parts, each corresponding to another change in the detector. These sets are labeled as Set A, Set B and Set C chronologically, as the detector evolved.

The cuts applied to the data for event construction must also be mentioned. As the TPC, the most basic cut is the requirement of only one cluster. The rest of the cuts are also similar, and can be found on Table 7.2.

Table 7.2. The general cuts and the corresponding conditions that the cuts are applied for the MicroMEGAS

Cut	**Condition**
Single Cluster	number of X clusters = number of Y clusters = 1
X multiplicity	$3 \leq$ number of anode hits ≤ 19
Y multiplicity	$3 \leq$ number of cathode hits ≤ 19
Energy Balance	Energy Deposition in Y $\approx 1.20\times$Energy Deposition in X
Coordinate Cut	Only events within the 14.5 cm^2 square shaped area centered on the middle are taken into account

The rest of the conditions vary for each of the data sets A, B and C. Also, the cuts are different for energies less than and greater than 4.5 keV. Table 7.3 shows these specific cuts applied to the different sets and to different energies.

Table 7.3. The cuts and the corresponding conditions that the are applied for the different data sets of MicroMEGAS

Set A Cuts	**Condition (E<4.5 keV)**	**Condition (E>4.5 keV)**
Rise Time	125.4 ns	126.043 ns
Pulse Length	614.9 ns	629.51 ns
RiseTime_over_PulseLength	0.2008	0.2001
Amplitude_over_PulseIntegral	3.1×10^{-3}	3.074×10^{-3}
RiseIntegral_over_PulseIntegral	0.2129	0.2073
RiseIntegral_over_DefaultIntegral	0.2132	0.2082
Set B Cuts	**Condition (E<4.5 keV)**	**Condition (E>4.5 keV)**
Rise Time	65.85 ns	68.446 ns
Pulse Length	314.419 ns	323.192 ns
RiseTime_over_PulseLength	0.2081	0.2108
Amplitude_over_PulseIntegral	6.15×10^{-3}	6.09×10^{-3}
RiseIntegral_over_PulseIntegral	0.2090	0.2125
RiseIntegral_over_DefaultIntegral	0.2434	0.2389
Set C Cuts	**Condition (E<4.5 keV)**	**Condition (E>4.5 keV)**
Rise Time	53.521 ns	57.173 ns
Pulse Length	306.785 ns	318.865 ns
RiseTime_over_PulseLength	0.1727	0.1777
Amplitude_over_PulseIntegral	6.18×10^{-3}	6.07×10^{-3}
RiseIntegral_over_PulseIntegral	0.1617	0.1735
RiseIntegral_over_DefaultIntegral	0.1849	0.1897

After the cuts are applied, the theoretical values for the axion spectrum are calculated and used in the event data to calculate χ^2. The rest of the calculation is exactly the same as the calculation for the TPC. However, the calculation is done for each of the sets, and the results are combined afterwards.

7.3.1. Online Analysis

The data area transferred from the VME crates to the computer via a National Instruments interface card and Labview software. All the online analysis programs are written by Labview.

One of the programs allows controlling the type of run (tracking, pedestal or calibration) and changes the high voltage and trigger accordingly. It can change the number of events per data file, change the position of the ^{55}Fe source, and as for monitoring, it can show the trigger rate and the number of events thus far recorded into the current data file.

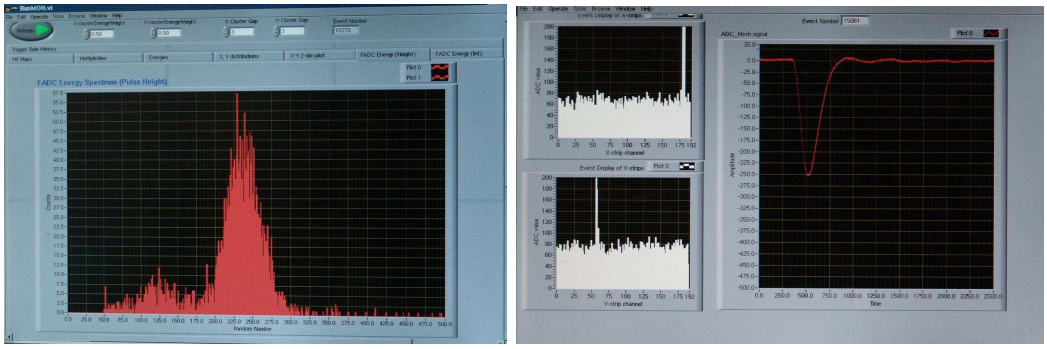

Figure 7.9. *Left*: The energy distribution graph of the online analysis of MicroMEGAS during calibration. The large peak is the 5.9 keV energy peak of ^{55}Fe calibration source, and the peak to the left, is the escape peak, which is 3 keV lower. *Right*: A typical photon signal of the online analysis program of MicroMEGAS. The two graphs on the left indicate the position of the signal in the X and Y strip numbers while the right graph indicates the energy deposition in the mesh as a function of time with respect to the trigger start

The other program is responsible solely for monitoring the signal observed by the detector. There are several tabs in the graphical interface (Figure 7.9L) which allow the shift person to observe the trigger rate history, hit maps, multiplicities, energies, the X-Y distributions - both by normal hits per channel in X (or Y) graphs and by 2-d

X vs. Y graph with color index for number of hits, FADC Energy and the integral of it. The FADC signal shape, the X and Y strip amplitudes can also be observed (Figure 7.9R).

7.3.2. Offline Analysis

The offline analysis for the MicroMEGAS detector was also completed only for the data of 2003. Eventhough the detector was changed in 2004, the basic principles are the same, so the analysis is similar. The changes in the detector structure affected the background directly, improving it dramatically (Figure 7.10). The overall background can be given as 4.82×10^{-5} photons/cm^2/sec/keV for the 2004 data.

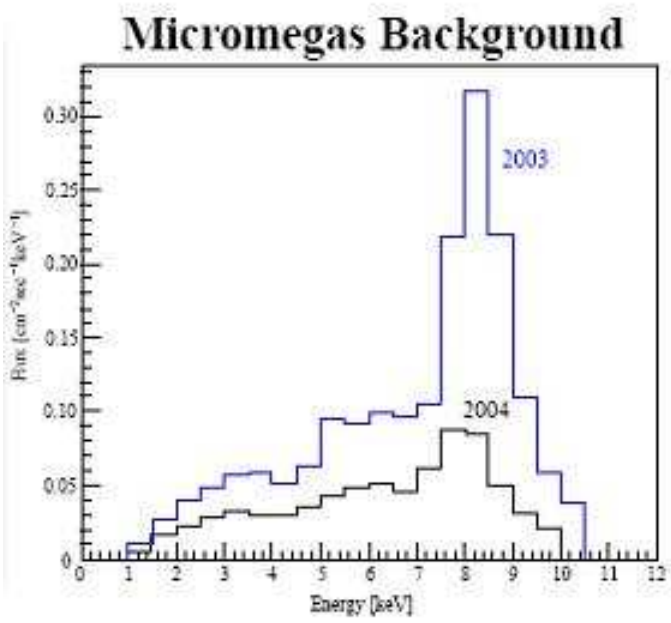

Figure 7.10. The improvement of background in 2004

When a signal coming directly from the cold bore is observed, it can be seen that only some parts of the detector volume is active (Figure 7.12). Therefore, this can be used as a cross check when a possible axion signal is observed, to see if it is actually coming through the bore or is an artifact. While this is not actively used in

the analysis, it certainly is something that one must know about, in order to make sure the genuinity of the signal, if there is one.

Of course, as with all the other detectors, MicroMEGAS also needs to be calibrated periodically. Although this is usually done with the online analysis program, the results should also be observed by the offline analysis, just for double checking, if for nothing else. The calibration data are used to calculate the energy that the FADC amplitude corresponds to (Figure 7.13). As usual, the ADC count refers to the deposited energy. The major peak should be calibrated as 5.9 keV as ^{55}Fe peak, while the small peak is the Ar escape peak with energy 2.9 keV. Again, as with the TPC, an ^{55}Fe source is used for calibration with the known 5.9 keV peak.

When the scaled down background and the tracking data for the 2003 data of MicroMEGAS detector are compared, no signal can be seen. While tracking counts indeed seem to be more than background at some points, this is within statistical uncertainty and at some other points background counts indeed seem to be more than tracking (Figure 7.14).

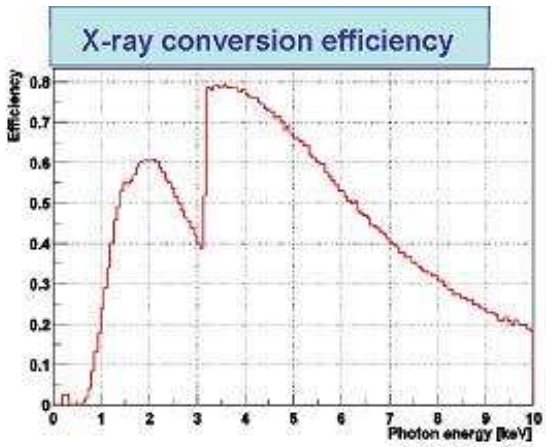

Figure 7.15. The x-ray conversion efficiency for the MicroMEGAS detector. Note the drop in efficiency at ∼3 keV

Like the TPC, the conversion efficiency drops near 3 keV for the MicroMEGAS

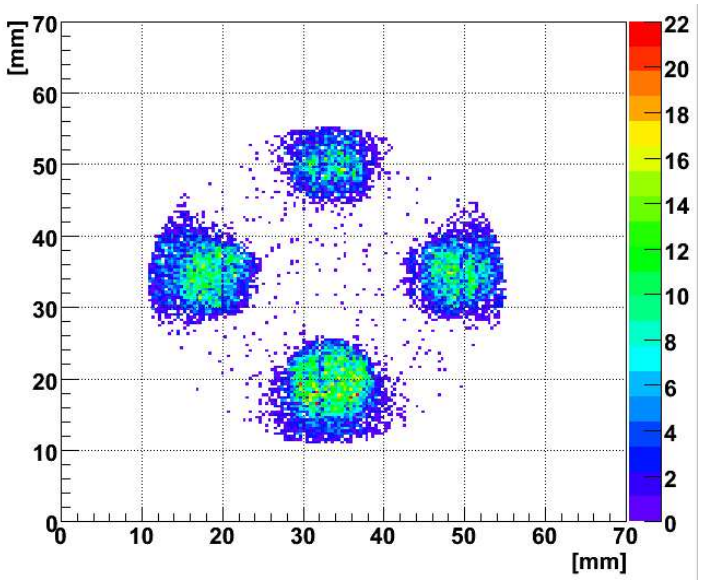

Figure 7.11. The X strip versus Y strips graph with events counts shown in color scale, during calibration procedure

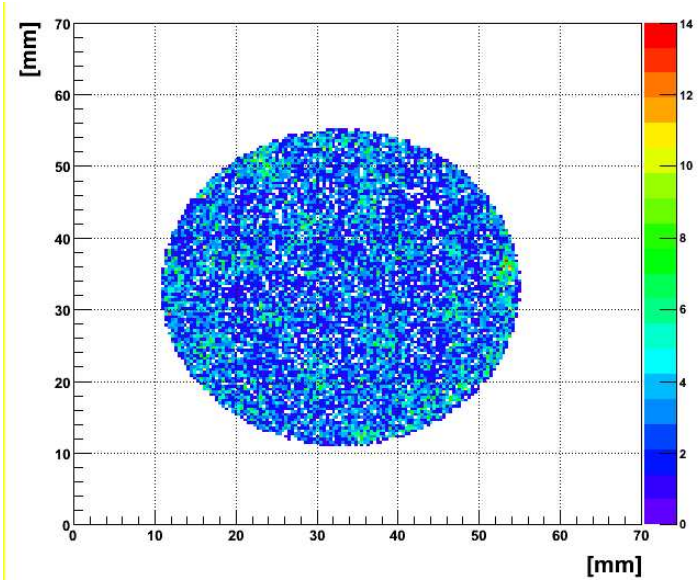

Figure 7.12. The X strip versus Y strips graph with events counts shown in color scale, during data taking procedure

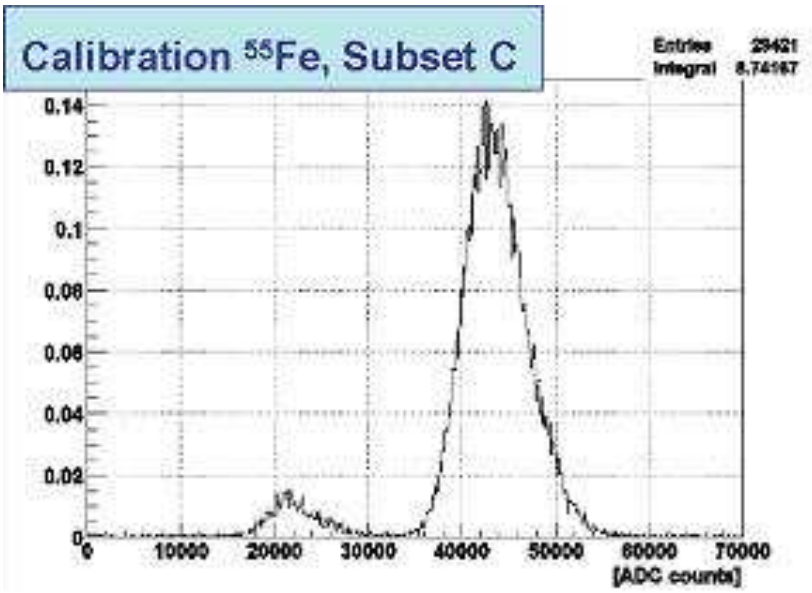

Figure 7.13. The calibration results as number of events per ADC counts

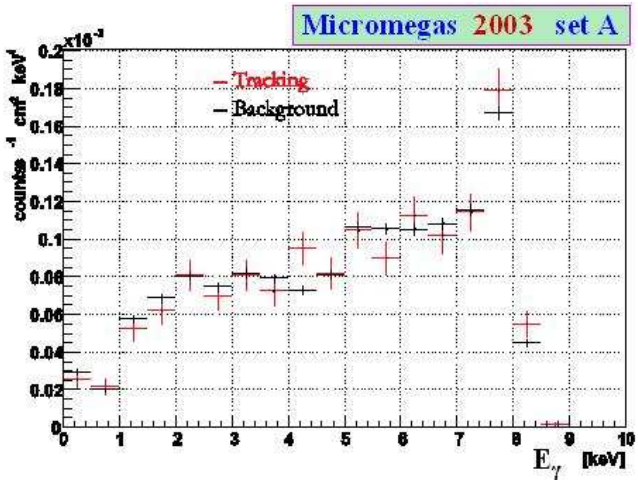

Figure 7.14. The background and tracking data comparison for the data of 2003 of MicroMEGAS detector

detector too, because of the usage of Ar within the volume of the detector (Figure 7.15). This is the same reason that the structure exists in the 95% CL upper limit on the expected values of $g_{a\gamma}$ in Figure 7.16. Besides from this expected phenomena, there is no signal observed in the 2003 data, as can be seen.

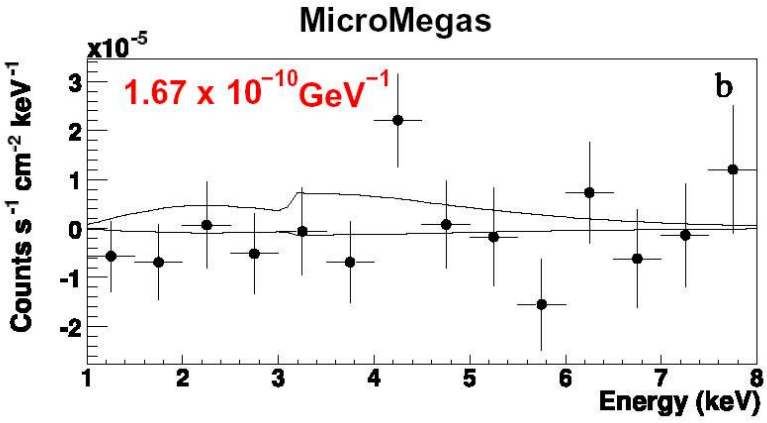

Figure 7.16. The results of the 2003 data set of the MicroMEGAS detector. The points are the background subtracted tracking data set, the lower line corresponds to the expectation for the best fit, while the higher line corresponds to the best fit with 95% CL upper limit. Note the structure at ∼3 keV due to efficiency

8. SUMMARY AND CONCLUSIONS

While only data for the 2003 period have been analysed, and no axion signal have been found so far, a better limit for the coupling constant have already been proposed from the analysed data:

$$g_{a\gamma} \leq 1.16 \times 10^{-10}\ GeV^{-1}. \tag{8.1}$$

The analysis of the 2004 data are still ongoing as this document is being prepared. The preperations being complete in December 2005, the Phase II has started taking data with one pressure step per day. The daily pressure steps are of 0.083 mbar each, and as of the end of data taking period of 2005, 19 pressure steps were completed, having scanned the pressure range up to 1.577 mbar.

While most of the changes proposed for Phase II have been completed before the data taking process has begun, newly arising problems forces the collaboration to find new solutions, even as the data taking is commencing. A probe to monitor the thermoacoustic oscillations have been installed in march, for example, and the tests have been completed in april. On the other hand, the results from this probe are yet to be analysed.

We have found a possible cause of the laser spot shift during the alignment procedure of 2005, and determined that it wouldn't produce a problem for the well-being of the experiment. The cause of the shift was probably the introduction of a gas inside the cold bore, with a diffractive index not equal to one, and the thrermal gradients within the bore.

The spots on the cold windows that we have thought solved have been apearing also, since the heaters cannot be turned on all the time, due to the conflict with the cryogenics. An optical system with mirrors and fiber optics was proposed that will

allow us to monitor the cold windows without having to take out the detectors; or heating the windows in specific time intervals (like every two weeks) were proposed, but even the question that whether the spots are harmful for the well-being of the experiment is still debatable.

All and all, the data taking is going smoothly, no matter what difficulties are faced, due to the dilligence and hard work of the collaboration members that have made the SR8 building their second home.

APPENDIX A: ABOUT THE GLUON GAUGE FIELD STRENGTH TENSOR

To lower the indices of $F^{\mu\nu}$, all one has to do is to multiply it with $\frac{1}{2}\epsilon_{\mu\nu\sigma\rho}$,

$$F_{\sigma\rho} = \frac{1}{2}\epsilon_{\mu\nu\sigma\rho}F^{\mu\nu}. \tag{A.1}$$

Let the a in $F^{a\mu\nu}$ represent the color factor. There are eight different values for a instead of nine, since the color group is an SU(3) group. If we think of the color of the quarks as an index, say α, then the quarks will be represented by U^{α} where α can take values 1, 2, 3, corresponding to the three colors. Therefore U^{α}, being the quark vector, transforms under SU(3) as,

$$U^{\alpha} \rightarrow M^{\alpha}_{\beta}U^{\beta}. \tag{A.2}$$

On the other hand, V_{α}, the covariant form, transforms under complex conjugate transformation,

$$V_{\beta} \rightarrow N^{\beta'}_{\beta}V_{\beta'}, \tag{A.3}$$

where, $\overline{M}^{\alpha}_{\beta} = N^{\beta}_{\alpha}$ i.e. $M^{\dagger} = N$, where † denotes the conjugate transformation. So, if we set the outer product as W^{α}_{β},

$$U^{\alpha}V_{\beta} = W^{\alpha}_{\beta}, \tag{A.4}$$

then it satisfy $W = W^{\dagger}$ and will trasform as,

$$W^{\alpha}_{\beta} \rightarrow M^{\alpha}_{\alpha'}W^{\alpha'}_{\beta'}N^{\beta'}_{\beta}, \tag{A.5}$$

and since $\overline{M}^{\beta}_{\beta'} = N^{\beta'}_{\beta}$, it actually only means,

$$W \to MWM^{\dagger}. \tag{A.6}$$

We can decompose W^{α}_{β} as,

$$W^{\alpha}_{\beta} = \delta^{\alpha}_{\beta}\frac{1}{3}trW + \tilde{W}^{\alpha}_{\beta}, \tag{A.7}$$

Since $trW = 3.\frac{1}{3}trW + tr\tilde{W}$, and $\tilde{W}^{\alpha}_{\beta}$ is traceless,

$$tr\tilde{W} = 0. \tag{A.8}$$

So, the W matrix is composed of 8 components which are,

$$\begin{aligned} W = W^1 \begin{pmatrix} 0 & 1 & 0 \\ 1 & 0 & 0 \\ 0 & 0 & 0 \end{pmatrix} + W^2 \begin{pmatrix} 0 & -i & 0 \\ i & 0 & 0 \\ 0 & 0 & 0 \end{pmatrix} + W^3 \begin{pmatrix} 1 & 0 & 0 \\ 0 & -1 & 0 \\ 0 & 0 & 0 \end{pmatrix} \\ + W^4 \begin{pmatrix} 0 & 0 & 1 \\ 0 & 0 & 0 \\ 1 & 0 & 0 \end{pmatrix} + W^5 \begin{pmatrix} 0 & 0 & i \\ 0 & 0 & 0 \\ -i & 0 & 0 \end{pmatrix} + W^6 \begin{pmatrix} 0 & 0 & 0 \\ 0 & 0 & 1 \\ 0 & 1 & 0 \end{pmatrix} \\ + W^7 \begin{pmatrix} 0 & 0 & 0 \\ 0 & 0 & -i \\ 0 & i & 0 \end{pmatrix} + W^8 \begin{pmatrix} 1 & 0 & 0 \\ 0 & 1 & 0 \\ 0 & 0 & -2 \end{pmatrix}. \end{aligned} \tag{A.9}$$

These components are called the Gell-Mann λ-matrices. The simple representation is:

$$W^{\alpha}_{\beta} = W^a(\lambda_a)^{\alpha}_{\beta}, \tag{A.10}$$

where a can take values from 1 to 8. These must correspond to the combinations of colors and anticolors. However there are 8 instead of the expected nine, which is caused by the truly colorless combination, i.e. $R\overline{R} + B\overline{B} + G\overline{G}$. The transformation leads to

the same combination, therefore we can say that this particular combination is not transformed.

APPENDIX B: VALVES, PUMPS AND PROBES OF CAST

CAST is a closely monitored experiment, as all experiments that have a similar large budget. Any lost data means that a certain measurement might have to be repeated, which would lead to loss of manpower, electricity, but most importantly precious time. Therefore, apart from the detectors, many variables of the system are monitored and controlled by a system of probes and valves. The data from these probes are stored by the slow control program, while also recorded manually especially during tracking. Although some of this recording might seem unnecessary, these reduntant data allow double checking and confidence in the slow control data.

The probes and the valves therefore all have been named according to where they are placed, and what they are measuring.

B.1. The Valves and Pressure Sensors

The CAST experiment relies heavily on the monitoring of the pressure. Because the refractive index on the gas is dependent on the density, and hence the pressure, the pressure inside the cold bore; because the magnet is operated at the limit of its functionality, all the other pressures have to be monitored precisely to prevent an error, like an error in the mass sweep in the axion search or an error that can damage the components of the magnet, the detectors or the telescope. For this reason several pressure sensors[31] have been placed throughout the cold bore and the gas lines (Figure B.2). The detectors' pressures are monitored by the sensors named after themselves: PTPC, PCCD and PMM; while the other sensors within the vacuum region are numbered: P1, P1BA on the TPC side of the TPC valves VT1 and VT2, P7, P7BA on the cold windows side of the same valves, P3, P3BA between the MicroMEGAS window and VT3, similarly P4, P4BA between the telescope and VT4, which are all monitored by the slow control. The sensors inside the ^{4}He region are directly connected to the pressure monitoring computer outside the control room, and are Pcold, Pnuno. The

[31] Maxigauge brand

Baratron100 and Baratron1000 sensors mentioned in Section 4.3.3 about pressure settings, are also connected to the same computer for monitoring. There are also several pressure sensors just for the CCD-Telescope system, but there are mentioned in Section 6.2 about the CCD, together with the pumps and valves network.

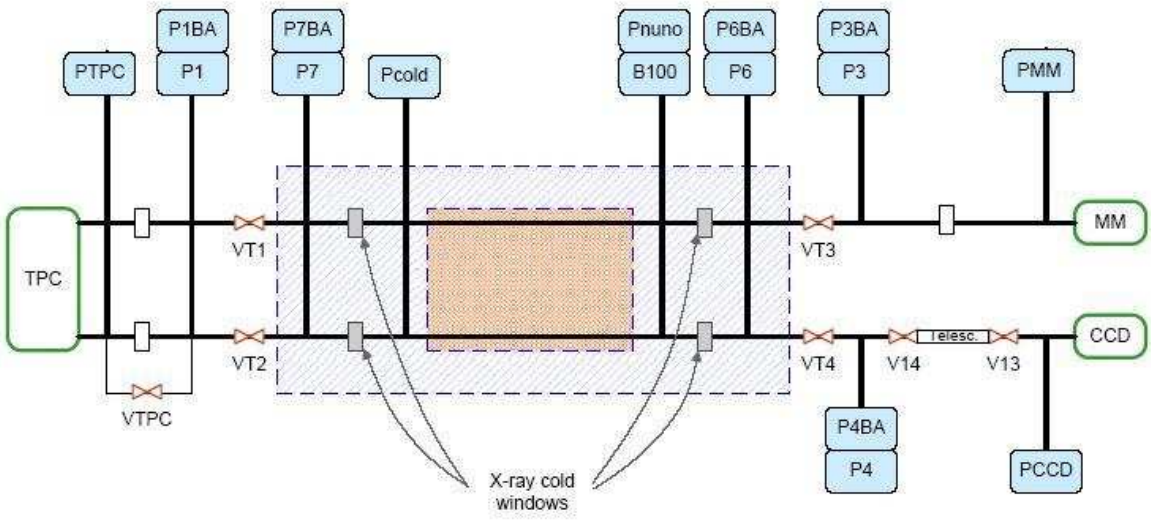

Figure B.1. The valves and the pressure sensors of the cold bore and the intermediate pipelines

The valves in the cold bore of CAST were inserted mainly as a safety feature, that is, in case of a quench or abnormal reading from the sensors, they all close down and prevent damage to the detectors. As can be seen in Figure B.2, there are several valves on the cold bore, preventing damage in case of a quench, and making the installing and removing of the detectors easier without disturbing the vacuum of the rest of the system. The main valves that are controlled from the main rack beside the telescope of CCD are VT1, VT2, VT3 and VT4. On the other hand, there are also other valves that are controlled from various places, like VT13 and VT14, which are controlled from the CCD pressure control computer; or VTPC which has a foolproof control system mounted close to the valve. In case VT1 and VT2 closes, the automatic opening of the VTPC makes sure that the windows are not damaged because of the pressure difference

that will accumulate.[32] A similar arrangement was also installed for MicroMEGAS window, not shown on the figure.

These valves are only some of the electronic valves which have to be monitored again electronically in order to make sure they are working correctly. There are also the manual valves all over the experiment, too numerous to mention all. For example the valves controlling the flow of ^{4}He into the cold bore have been mentioned in section 4.3.3 about the pressure settings; not to mention all the valves that are connected between the vacuum regions and the pumps.

B.2. The Pumps

Since CAST is an experiment that needs vacuum for its operations, several vacuum pumps are at its disposal. Most of them are oil pumps, but some of them happen to be dry pumps. While most of them are turbo pumps, some of them happen to be two stage pumps. Most of them are always connected to the system, but some of them are connected only from time to time.

It is obvious why the pumps that are connected from time to time should be two stage pumps, since the connection process itself is something which destroys the vacuum, and the two stage pumps (Bonjon pumps in CAST) are the only pumps that can start operation at high pressure ($\sim$1 atm). Basically the turbo pump in the two stage pump is connected to the system only after it reaches a certain rotation speed, i.e. when a certain vacuum value is reached. Therefore, these are the pumps that are used when a region is to be pumped for the first time. After a certain vacuum value is reached, the turbo pumps mounted on the magnet can be started.

There are several of these turbo pumps that are mounted, for protection of the detector windows, and for ensuring the vacuum of the telescope etc. The pump that is ensuring the vacuum of the cold bore is a dry pump, with no danger of oil leaks,

[32] Since while P1 cryopumped, PTPC is only pumped by the turbo pump, and this therefore increases pressure difference.

Figure B.2. *Left*: The Bonjon pump. *Right*: The differential pumping station

there are three pumps for the Telescope-CCD system, one for the TPC, connected behind the window, and one for the MicroMEGAS connected similarly. The TPC and MicroMEGAS pumps are named as differential pumps, for they ensure that the intermediate region is in relatively poor, but high enough vacuum to keep diffusion through the detector windows to a minimum.

REFERENCES

1. "Chronologie du CERN et de Wolfgang Pauli", *CERN - Scientific Information Service - Archive.*

2. Aalseth, C.E. *et. al.*, "A Solar Axion Search using a Decommisioned LHC Test Magnet", *CERN 99-21 SPSC/P312*, 9 August 1999.

3. Beltrán, B., "SEARCH FOR SOLAR AXIONS: THE CAST EXPERIMENT AT CERN" - The CAST Collaboration, *arXiv:hep-ex/0507007* Vol.1, 1 Jul 2005.

4. Peccei, R.D., Quinn, H.R., "CP Conservation in the Presence of Pseudoparticles", *Physical Review Letters*, Vol.38, No.25, pp.1440, 1977.

5. Minowa M., Moriyama S., Inoue Y., Namba T., Takasu Y., Yamamoto A., "The Tokyo Axion Helioscope Experiment", *arXiv:hep-ex/9806015*, Vol.1, 16 June 1998.

6. Avignone F.T. *et. al.*, "Experimental search for solar axions via coherent Primakov conversion in a germanium spectrometer" - The SOLAX Collaboration, *arXiv:astro-ph/9708008*, Vol.1, 1 Aug 1997.

7. Morales, A. et al, "Particle Dark Matter and Solar Axion Searches with a small germanium detector at the Canfranc Underground Laboratory" - The COSME Collaboration, *arXiv:hep-ex/0101037*, Vol.1, 22 Jan 2001.

8. Zavattini E. *et. al.*, "PVLAS : probing vacuum with polarized light" - PVLAS collaboration, *arXiv:hep-ex/0512022*, July 2005.

9. Asztalos S.J. *et. al.*, "An improved RF cavity search for halo axions" - The ADMX Collaboration, *arXiv:astro-ph/0310042*, 2004.

10. Sikivie P., "Detection Rates for "invisible" axion searches", *Physical Review D*, Vol.32, No.11, pp.2988, 1985.

11. Csáki C. *et. al.*, "Dimming Supernovae without Cosmic Accelerartion", *Phys. Rev. Letters* Vol.88 No.16, 22 April 2002.

12. Sikivie P., "Experimental Tests of the "Invisible" Axion", *Phys. Rev. Lett.* Vol.51, pp.1415, 17 October, 1983.

13. Bibber K. van, *et. al.*, "Design for a Practical Laboratory Detector for Solar Axions", *Physical Review D*, Vol.39 No.8 pp.2089, 15 April 1989.

14. Bahcall, John N. *et. al.*, "Solar models and solar neutrino oscillations", *arXiv:hep-ph/0404061* Vol.1, 6 Apr 2004.

15. Zioutas, K., "Astrophysical signatures for Astrophysical signatures for axion axion(-like) particles", ILIAS ILIAS-CAST CAST-CERN CERN Axion Axion Training, CERN / Geneve, 30 November 2005.

16. Bottura, L. *et. al.*, "Field Quality of the LHC Dipole Magnets in Operating Conditions", *Proceedings of EPAC 2002*, Paris, France.

17. Kuster, M. "Axion Search - CAST", *Astroteilchenphysik in Deutschland: Status und Perspektiven 2005*, DESY, Zeuthen, 4 October 2005.

18. Vogel, J., "The Precision of the Tracking System in Search of Solar Axions", *PhD Thesis for Kakultät für Mathematik und Physik Albert-Ludwigs-UNiversität Freiburg im Breisgau*, December 2005.

19. Ruz, J. *et. al.*, "Background Shielding for the TPC of the CAST Experiment", September 2005

20. Knoll, G. F., "Radiation Detection and Measurement", *John Wiley & Sons*, pp.707, 1989.

21. CAST Collaboration, "Status Report of the CAST Experiment", *1CERN-SPSC-2004-019*, SPSC-M-718, 30 June 2004.

22. Kuster, M. *et. al.*, "pn-CCDs in a Low-Background Environment: Detector Background of the CAST X-ray Telescope", *arXiv:physics/0508064*, Vol.1, 10 August 2005.

23. *http://cast.mppmu.mpg.de*

24. Zioutas, K. *et. al.*, "First results from the CERN Axion Solar Telescope (CAST)", *arxiv:hep-ex/0411033* Vol.2 01 March 2005.

25. Kuster M., Bräuninger H., Dogan B. O., Joux J. N., Kotthaus R., Lippitsch A., "Telescope Alignment for Phase II of CAST", *CAST Scientific / Technical Report: CSTR-05-002*, 22 November 2005.

26. Andriamonje, *et. al.*, "First Results From The CERN Axion Solar Telescope (CAST)", *IDM2004 Conference Procdeedings*, 26 November 2004.

27. "Data Treatment of the TPC Data" - TPC group, TPC analysis report, 2003.

28. Kuster, M., "Data Analysis Repot – pn-CCD" - CCD group, *CAST Scientific / Technical Report: CSTR-04-001*, 23 August 2004.

29. Dafni, T., "The Analysis of the Micromegas Detector for the 2003 data" - Micomegas group, CAST internal note, 14 August 2004.

30. Fanourakis G.K., *et. al.*, "The use of the Micromegas technology for a new imaging system", *Nuclear Instruments and Methods in Physics Research*, 2004.

31. Andriamonje S., *et. al.*, "A Micromegas detector for the CAST experiment", *Nuclear Instruments and Methods in Physics Research*, 2004.

32. Dafni, T., "Pulse Shape Analysis", "Presentation for the 3rd Analysis Meeting of CAST", 7 September 2003.